JKU

**JOHANNES KEPLER
UNIVERSITY LINZ**

Submitted by
Stepan Demchyshyn
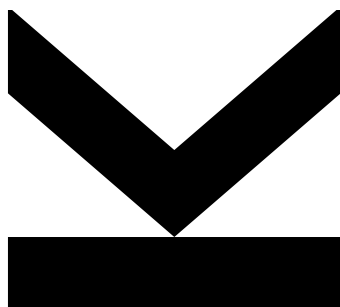
Submitted at
**Linz Institute for Organic Solar Cells
Institute of Physical Chemistry**

Supervisor
Assoz. Univ.-Prof. DI Dr. Markus Scharber

Co-Supervisor
Assoz. Univ.-Prof. DI Dr. Martin Kaltenbrunner

June 2018

Quantum confinement effects for light emission in perovskites

Master Thesis

to obtain the academic degree of

Diplom-Ingenieur

in the Master's Program

Technische Chemie

Contents

Declaration

I hereby declare that the thesis submitted is my own unaided work, that I have not used other than the sources indicated, and that all direct and indirect sources are acknowledged as references. This printed thesis is identical with the electronic version submitted.

Linz, June 2018

To my little brother Nazar and my whole family for their immense support.

Acknowledgment

I would like to thank Markus Scharber for supporting me during my thesis work both practically and intellectually as well as o.Univ.Prof.Mag.Dr.DDr.h.c.Niyazi Serdar Sariciftci for his support and encouragement during the whole duration of my work at Linz Institute for Solar Cells (LIOS)/ Institute of Physical Chemistry. Especially I would like to express my gratitude to my supervisor Martin Kaltenbrunner who guided me, was a great teacher, and a good friend throughout the time of PC3 praktikum and this master thesis.

Additionally, I would like to acknowledge the help of Eric Głowacki for supporting and introducing me to the world of material science at the very beginning of my work at LIOS. Special thanks to Maria Jakesova and Dominik Farka who shared with me their memorable experiences at LIOS and brought me into the community. I would like to thank Dogukan Apaydin for helping me navigate through the day-to-day science "forest" and being an excellent friend. Thanks to Christoph Ulbrich and Herwig Heilbrunner for their practical support and many long discussions which always guided me in the right way. I am also very grateful Prof. Siegfried Bauer for invaluable discussions concerning various parts of the research topic as well as for being ever-so supportive and encouraging.

None of the work would be possible without constant support fromn Patrick Denk, Gerda Kalab and Gabriele Hinterberger who helped me with all possible technical issues and answered all of my questions. Of course, I would also like to thank Sarah Gusner, Birgit Paulik, Isolde Wandling, and Christa Mitschan who at any point were extremely helpful when it came to administrative and bureaucratic support. Furthermore, I would like to thank the whole LIOS team for being supportive and creating amazingly genial environment inside and outside the laboratory.

Also I would like to thank Janina Roemer and Prof. Bert Nickel from Ludwig-Maximilian University in Munich, who helped with structural analysis and carried out experiments in at synchrotron beamline at Deutsches Electronen-Synchrotron (DESY) in Hamburg with the help of Uta Rütt and Florian Bertram. Great thanks to Cezarina Mardare for her help with thin film

XRD analysis and help with the interpreting the results of the experiment. Also I would to thank Heiko Groiss and Günter Hesser from ZONA (Zentrum für Oberflächen- und Nanoanalytik), JKU for their help with SEM and TEM imaging.

Abstract

Research in halide perovskites has been dominated over the last few years by solar cells, now also includes a growing focus on this materials light emitting properties. Halide perovskites are an appealing group of materials due to their high performance, simple synthesis route, and low price. Recent advances in colloidal perovskite quantum dot synthesis allow to easily tune optical and electronic properties based on quantum size effects. In this work, a new method utilizing porous oxide materials is investigated for lead based hybrid organic-inorganic perovskite quantum dot preparation. Optical properties of perovskites confined in porous oxide matrices are studied and correlated with their detailed structural analysis. The behavior of charge carriers in this new material is investigated via low temperature spectroscopy. Light Emitting Diodes (LEDs) based on the material are prepared. Additionally, a non-lead based perovskite material is investigated as a potential non-toxic alternative quantum confined material. This new approach to perovskite quantum dot synthesis opens up further compelling avenues for research on the fundamental properties of quantum confined particles as well as development of new optoelectronic devices.

Kurzfassung

Solarzellen dominieren im Wesentlichen die Forschung im Bereich der Halogen-Perowskite. Erst vor kurzem rückten die lichtemittierenden Eigenschaften dieser Materialklasse stärker in den Fokus und gewinnen seitdem stark an Bedeutung. Halogen-Perowskite sind eine hochaktuelle und attraktive Gruppe von Materialen aufgrund ihrer hohen Effizienz, einfacher Synthese und niedrigen Preises. Neueste technologische Fortschritte in der Synthese von kolloidalen Quantenpunkten ermöglichen die Feinabstimmung der optischen und elektrischen Eigenschaften durch größenabhängige Quantisierungseffekte. In dieser Masterarbeit wird eine neue Methode für die Herstellung von bleihaltigen organisch-anorganischen Perowskit Quantenpunkten unter der Verwendung von porösen Metalloxidstrukturen aufgezeigt. Die optische Eigenschaften von innerhalb poröser Oxidmatrizen eingeschlossenen Perowskiten wurden untersucht und mit einer ausführlichen strukturellen Analyse korreliert. Das Verhalten der Ladungsträger in diesem neuen Material wurde mittels Tieftemperaturspektroskopie analysiert. Die so hergestellten Perowskit-Quantenpunkte finden praktische Anwendung als aktive, lichtemittierende Schicht in LEDs. Zusätzlich wurden Kupfer-Perowskite als bleifreie, möglichst wenig toxische alternative synthetisiert und auf ihre lichtemittierenden und strukturellen Eigenschaften untersucht. Dieses neue, allgemeine Konzept der Quantenpunkt Synthese eröffnet erfolgversprechende Wege sowohl in der Grundlagenforschung an Quantenpunkten als auch in der Entwicklung von zukünftigen optoelektronischen Bauteilen.

1 Introduction

1.1 Quantum confinement

The Schrödinger equation lies at the heart of quantum mechanics theory and helps to explain a number of chemical and physical phenomena [1]. Generally, the equation can be written as

$$\hat{\mathcal{H}}\psi = E\psi \tag{1.1}$$

where $\hat{\mathcal{H}}$ is the Hamiltonian operator, ψ is the wavefunction, and E is the energy of the system. This equation can be expanded to its full form in the following way

$$-\frac{\hbar^2}{2m}\nabla^2\psi + U\psi = E\psi \tag{1.2}$$

where $\hbar$ is the reduced Plank constant, m - mass of a particle that is being examined, $\nabla^2 = \frac{\partial^2}{\partial^2 x} + \frac{\partial^2}{\partial^2 y} + \frac{\partial^2}{\partial^2 z}$ - second partial derivative over all the spacial dimensions, and U - potential energy, that depends on the particle's position.

The Schrödinger equation also accounts for the quantization of energy, meaning that the energy of a particle can assume only certain allowed values. This phenomena can be explained by setting-up a thought experiment, where an electron is trapped inside a one dimensional potential energy box (Fig.1.1). A time independent Scrödinger equation is constructed to describe this situation for an electron with a mass m, moving with energy E in one dimension as follows

$$-\frac{\hbar^2}{2m}\frac{d^2}{dx^2}\psi + U(x)\psi = E\psi \tag{1.3}$$

The boundary conditions (eq.1.4) for a particle in a box problem help to clarify the behavior of the electron as well as to solve the equation. The electron cannot move outside of the box, due to the fact that the walls have infinitely high potential, but it can move freely within the confined space of the box, since the potential energy inside equals 0

$$U(x) = \begin{cases} 0, & if \quad 0 < x < L \\ \infty, & otherwise \end{cases} \tag{1.4}$$
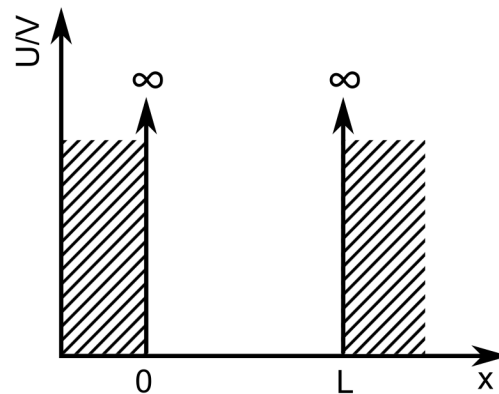
Figure 1.1: Schematic description of a one-dimensional box with potential $x < 0 < L$ and walls that have infinitely large potential.

Considering 0 potential inside the box, eq.1.3 can be further simplified to

$$-\frac{\hbar^2}{2m}\frac{d^2\psi}{dx^2} + U(x)\psi \overset{0}{=} E\psi \tag{1.5}$$

and the complete solution to this equation is obtained, consisting of its eigenfunction (wavefunction ψ) and the corresponding eigenvalue (energy E)

$$\psi_n(x) = \left(\frac{2}{L}\right)^{1/2} sin\left(\frac{n\pi x}{L}\right), \quad for \quad 0 \leq x \leq L \tag{1.6}$$

$$E_n = \frac{n^2 h^2}{8mL^2}, \quad n = 1, 2, ... \tag{1.7}$$

One of the most notable consequences of this solution is the emergence of the quantum number n which can only assume a positive integer values. This allows for only certain energy levels to be occupied by an electron (quantization), whereas classically, electrons can occupy any energy. The quantum number n often is used to refer to the state corresponding to the energy and to explicitly express the wavefunction equation.

A particle in a box problem is also an excellent model for behavior of electrons and holes in quantum confined materials, like quantum wells, wires and dots [2]. A classical example of a quantum well is a structure in which a layer of a small band gap semiconductor is sandwiched between two layers of a large band gap semiconductor (Fig.1.2A) (for example a layer of GaAs between two layers of AlGaAs). In this arrangement electrons are confined in one dimension (x) but are free to move in other two (y and z). In order to observe quantum confinement effects in this structure, the thickness of the layer in the x dimension should be of the same order of magnitude as the wavelength of the electron wavefunction [3]. In this case the energy spectrum
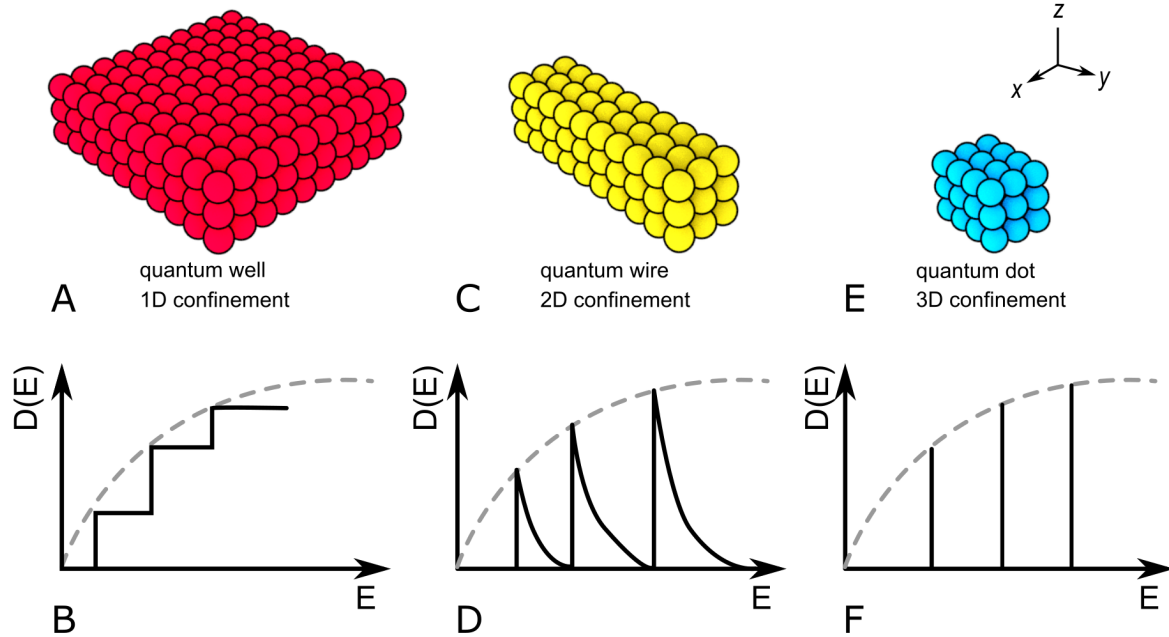
z

x   y

quantum well
1D confinement

A

quantum wire
2D confinement

C

quantum dot
3D confinement

E

D(E)

E

B

D(E)

E

D

D(E)

E

F

Figure 1.2: Illustration of various confinement cases and corresponding density of states functions $[D(E)]$. $D(E)$ for non-confined electron is shown as dashed gray lines in each of the respective graphs. (A) - quantum well structure in which electrons are confined only in one dimension (z); (B) - density of states in a 1D confinement case grows stepwise as the energy increases; (C) - quantum wire, in which electrons are confined in two spatial dimensions (z and x); (D) - density of states of 2D confined structure showing sharp peak-like values which then rapidly decay; (E) - quantum dots, structures in which electrons are confined in all three dimensions (z, x, y); (F) - $D(E)$ in quantum dot materials is a series of δ functions at each allowed energies, meaning that it has non-zero values only at discrete E values. Figure adapted from [2].

becomes discrete. The total energy of an electron in a quantum well can be described with the following equation

$$E_{n,k_x,k_y} = \underbrace{E_C}_{\text{conduction band}} + \underbrace{\frac{n^2 h^2}{8 m_e^* L^2}}_{\text{confined}} + \underbrace{\frac{\hbar^2 (k_x^2 + k_y^2)}{2 m_e^*}}_{\text{non-confined}} \tag{1.8}$$

where the first part of the equation comes from the energy of the conduction band, the second part is given by the particle in a box model for one dimensional confinement and the last part is contributed by two other dimensions which are not confined and can be calculated by the effective mass approximation. Another important consequence of quantum confinement is the modification of the density of states, $D(E)$, which can be defined as number of energy states between E and $E + dE$. For a bulk semiconductor $D(E)$ rises with $E^{1/2}$, whereas in a quantum well, $D(E)$ is a stepwise function shown in Fig.1.2B and is described with the following equation

$$D(E)_{well} = m_e^*/\pi^2 \tag{1.9}$$

The stepwise behavior results in high $D(E)$ near the band edge, when compared to the bulk

semiconductor. This contributes to increased strength of optical transitions and high oscillator strength.

The idea of one-dimensional confinement can be expanded to two-dimensionally confined structures, so-called quantum wires (Fig.1.2C). In manner similar to quantum wells, the electron energy in a quantum wire can be calculated using the following equation

$$E_{n_1,n_2,k_y} = \underbrace{E_C}_{\text{conduction band}} + \underbrace{\frac{n_1^2 h^2}{8m_e^* L_x^2}}_{\text{confined}} + \underbrace{\frac{n_2^2 h^2}{8m_e^* L_z^2}}_{\text{confined}} + \underbrace{\frac{\hbar^2 k_y^2}{2m_e^*}}_{\text{non-confined}} \tag{1.10}$$

which has a contribution of conductive band energy, confinement in two dimensions (one for x and one for z), and effective mass approximation for one dimension in which the electrons can move freely (y). The $D(E)$ profile of a 2D confined structure shows initial sharp peak at discrete E values and then decreases as E increases (Fig.1.2D). This relationship can be described with the following equation

$$D(E)_{wire} \propto (E - E_{n1,n2})^{1/2} \tag{1.11}$$

Singularity-like sharp peaks at discrete E positions close to the band gap edge again cause an increase in optical transitions, which is even stronger than can be observed in quantum wells. Additional dimensions in which electrons and holes are confined also increase exciton binding energy, which is a characteristic property of quantum confined structures.

Some of the most interesting confined structures are the quantum dots. They limit electron movement in all 3 spacial dimensions resulting in energy levels becoming discrete in all of these 3 dimensions. One can refer to quantum dots as "artificial atoms", due to similarly discrete energy level distribution in real atoms. The amount of atoms inside a quantum dot can be anywhere from hundredths to several thousands and it can be produced in various geometrical shapes. Allowed energies for this structure can be calculated with the equation below

$$E_n = \frac{h^2}{8m_e} \left[\left(\frac{n_x}{L_x} \right)^2 + \left(\frac{n_y}{L_y} \right)^2 + \left(\frac{n_z}{L_z} \right)^2 \right] \tag{1.12}$$

$D(E)$ consists of δ-functions or sharp peaks (Fig.1.2F) which are evident even at room temperature and can be described with the following equation

$$D(E)_{dot} \propto \sum_{E_n} \delta(E - E_n) \tag{1.13}$$

The surface-to-volume ratio in the case of quantum dots is very large, which results in increased influence of surface defects on the properties of the material.

The behavior of quantum dots can be also analyzed considering excitons as basic particles confined within a radius R, since they are more relevant to the photoluminescent and other properties of the material [1]. The limiting size factor now becomes the exciton Bohr radius, or the distance between an electron-hole pair. In this case the Hamiltonian is constructed in the following way

$$\hat{\mathcal{H}} = -\frac{\hbar^2}{2m_e}\nabla_e^2 - \frac{\hbar^2}{2m_h}\nabla_h^2 + U(\boldsymbol{r}_e, \boldsymbol{r}_h) \tag{1.14}$$

where m_e and m_h is mass of the electron and hole respectively, $\boldsymbol{r}_e$ and $\boldsymbol{r}_h$ are positions of the electron and hole within the quantum dot. Coulomb interaction between the electron (charge $-e$) and the hole (charge $+e$), can be further expanded into the equation

$$U(\boldsymbol{r}_e, \boldsymbol{r}_h) = -\frac{e^2}{4\pi\epsilon|\boldsymbol{r}_e - \boldsymbol{r}_h|} \tag{1.15}$$

with ϵ being the permittivity of the medium and $|\boldsymbol{r}_e - \boldsymbol{r}_h|$ the distance between the electron and the hole. As a result of solving the Schrödinger equation, the energy of an exciton can be expressed in the following equation

$$E_{ex} = \frac{h^2}{8R^2}\left(\frac{1}{m_e} + \frac{1}{m_n}\right) + \frac{1.8e^2}{4\pi\epsilon R} \tag{1.16}$$

from which it is evident that the energy of an exciton decreases with increasing particle radius.

A number of other material properties also become a function of quantum dot radius, most significantly the band gap energy, E_g. Band gap tuning allows to control materials color and also the color of light emitted upon exciton recombination. This is an especially useful property in applications like molecular labels and light emitting diodes (LEDs).

1.2 Porous silicon

Si is a metallic gray element that has been essential to humanity since early history in the form of silicon oxide for glass making and flint tools. Now it has become the centerpiece of the modern electronics industry, since >95% of electronics is Si based. Si has 4 valence electrons, two in the 3s and two in the 3p orbital [4]. It is a semiconducting material, with high resistivity that can be brought down 9 orders of magnitude by an addition of dopant elements like B, Al, P, *etc* [5]. Besides being widely used in its pure form in electronics, there is a significant interest in micro- and nanostructuring of Si surface through various techniques. Some of the methods include electrochemical, photoelectrochemical, electroless, galvanic, metal assisted, and vapor etching [6].
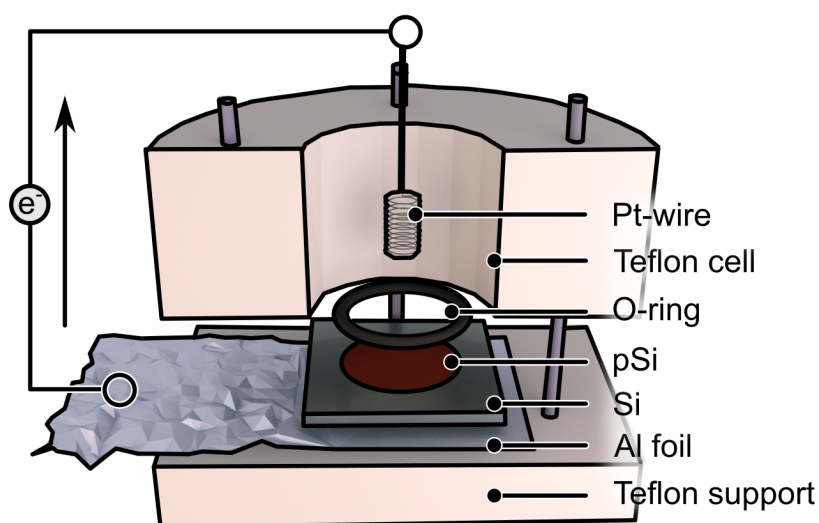
Figure 1.3: Electrochemical set-up used for pSi preparation. The cell consists of a square piece of Si wafer with an Al foil back contact sandwiched between two pieces of Teflon. A cylindrical opening on the top allows to introduce the electrolyte and a Pt-wire. When electrically connected, the reaction will occur on Si (anode, eq.1.18) and the Pt-wire (cathode, eq.1.17). Figure adapted from [6].

Porous silicon (pSi) was first discovered in 1950s by Uhlir during his work at Bell Laboratories [7]. The 1956 publication in *The Bell System Technical Journal*, details procedures for an electrolytic shaping of Ge and Si. Only at the very end of the paper there is a mentioning of "matte black, brown or red deposits" on the Si wafer when etched at low currents in HF electrolyte. The "deposit" has not been identified as pSi but the discovery slowly nudged the curiosity for the new material. In 1991 Lehmann and Gössele described quantum confinement effects of Si sandwiched in between pSi walls [8]. This generated a lot of interest for preparation of different devices (diffraction gratings [9], LEDs [10], *etc.*) and significantly spiked the interest in pSi. Another milestone discovery was made in 1995 by Canham, where he described *in vitro* studies of pSi in simulated physical fluids [11]. Both of these discoveries kick-started the field that has been on the rise now for the last 65 years.

The most common method of fabricating pSi is electrochemical etching of polished Si wafers in an HF/ethanol mixture. The classical set-up described by Sailor is shown in Fig.1.3, where the Si wafer serves as the anode and a Pt wire is the cathode. Two types of reactions can occur during the procedure depending on the current density applied. At high current density a 4-electron reaction takes place, which initiates the electropolishing regime, where layers of Si are removed homogeneously from the wafer surface and no pSi is formed.

On the other hand, at low current density a 2-electron reaction prevails yielding a pSi struc-

ture. During the 2-electron reaction the usual hydrogen formation proceeds on the cathode
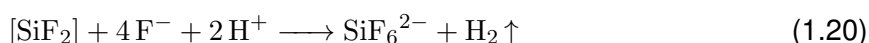
$$2\,H^+ + 2\,e^- \longrightarrow H_2\uparrow \tag{1.17}$$

whereas at the anode there is a dissolution of Si into $SiF_6{}^{2-}$, and surprisingly, also an evolution of H_2

$$Si + 6\,F^- + 2\,H^+ + 2\,h^+ \longrightarrow SiF_6{}^{2-} + H_2\uparrow \tag{1.18}$$
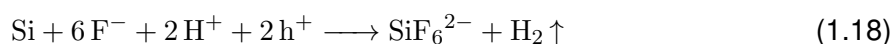
The last equation can be broken down into two separate reactions, one of which is of electro-chemical nature

$$Si + 2\,F^- + 2\,h^+ \longrightarrow [SiF_2] \tag{1.19}$$

and the other one of chemical

$$[SiF_2] + 4\,F^- + 2\,H^+ \longrightarrow SiF_6{}^{2-} + H_2\uparrow \tag{1.20}$$

Even though the process of pSi formation is not trivial and has been shown to depend on a number of factors (temperature, electrolyte composition, illumination intensity, Si wafer dopant type and amount [6]), the most important factors are current density and anodization time. Within the appropriate current density regime, higher current density will result in larger pores, larger pore size distribution, and increased film porosity [12]. Longer anodization times will result in thicker pSi layers [13]. Furthermore, the pore propagation direction can be controlled via the crystallographic orientation of the Si wafer (100, 111 [14], 110 [15]). pSi sizes are classified into micropores that have diameter <2 nm (smallest diameter achieved 0.8 nm [16]), mesopores that range between 2 and 50 nm, and macropores that are 50 nm and larger [17]. Additionally, pSi under certain etching conditions can assume a hierarchical architecture (Euclidian or fractal-like geometry), meaning that mesopores can have branching micropores within themselves.

pSi finds use in a variety of fields including electronics, optics, catalysis, medicine, food, and cosmetics [18]. Nowadays, most of the research in pSi is conducted in the fields of battery research as pSi anodes [19], drug delivery [20], and biosensing [21]. Infiltration of pSi with different materials including polymers [22], metals and their oxides [23], carbon [24], biomolecules [25] has been investigated in depth. Due to its high surface area pSi has also been used for nanoexplosives [26], gas sensing [27], and gettering [28]. The number of applications of pSi serves as a testimony to the versatility of this material.

1.3 Porous alumina

Aluminum is the most abundant metallic element on Earth and also one of the most recently isolated. It is due to the fact that Al occurs in a combination with other elements and it has to be processed using large amounts of energy to separate and purify it [29].

The oxide of aluminum has been known since V century BC under various names (alumen, alumina, corundum, *etc.*). 90% of Al is used in industry to produce high quality Al alloys, while some is used in a form of aluminum oxide for applications in abrasives, adsorbents, catalysts, ceramics and refractories [30]. A thin passivation layer of aluminum oxide appears on the surface of Al metal immediately upon exposure to an ambient atmosphere, resulting in excellent wear and corrosion resistance of the material.

Electrochemically grown planar and porous anodic aluminum oxide (AAO) finds a number of applications in surface science and industry [31]. An early application of planar AAO was in seaplanes as body corrosion protection [32]. Porous AAO (pAAO) found its use in later industrial developments such as a substrate for electroplating or painting and is often found in electronic gadgets, cookware, cars, and architectural design [32]. However, nanoscience has not been utilizing the compelling properties of pAAO until 1995, when Masuda published his work on ordered pAAO [33], [34].

Both planar non-porous barrier type AAO (Fig.1.4A) and pAAO (Fig.1.4B) morphologies can be achieved via anodization. Neutral and lightly acidic electrolytes containing citric, boric, oxalic, phosphoric, adipic, and tungstic acid (pH 5-7) yield planar oxides, whereas strongly acidic electrolytes such as oxalic, sulfuric, phosphoric, chromic, and tartaric acid will produce pAAO [32]. In spite of the same chemical composition (Al_2O_3), the growth of planar and pAAO exhibits characteristic differences. The current density (j) profile under potentiostatic conditions of planar AAO will have decreasing j over time due to the insulating properties of planar AAO (Fig.1.4C). However, pAAO will have a stable j for a period of time of pore formation (Fig.1.4C).

Secondly, planar AAO grows simultaneously at the metal-oxide and oxide-electrolyte interfaces, while pAAO oxide forms at the metal-oxide interface only due to the migration of O^{2-}/OH^{-} ions towards the anode. In pAAO, Al^{3+} ions are ejected into the solution and do not contribute to the growth of the oxide. Yet another distinct feature of pAAO is the roughness of the initially formed oxide layer. In planar AAO, the initial layer tends to be uniform and is often observed to smoothen the substrate surface as the oxide grows. On the contrary, initial barrier oxide formed during pAAO anodization is greatly uneven, forming valleys and hills on
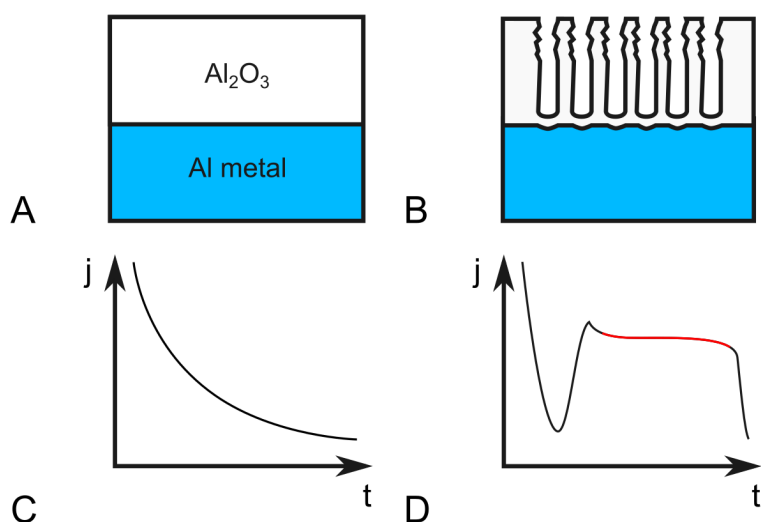
Figure 1.4: Schematic illustration of planar (A) and porous (B) AAO. Under potentiostatic anodization, planar AAO shows steady decay of current density as the oxide layer grows (C), while pAAO display a distinct region of stability for the duration of pore growth (highlighted in red) (D). Figure adapted from [32]

its surface. One of the theories explaining the mechanism of pAAO formation suggests that the rough barrier oxide created at the beginning of the anodization gives rise to the incipient pores due to electric field concentration in AAO valleys [35]. After a certain time of anodization, randomly distributed incipient pores will start to grow into larger ones, which will eventually align, assuming equilibrium morphology. The fact that the pores are aligned into ordered domains only at the bottom, is used in two step anodization, where the initial pAAO layer is dissolved and the anodization is repeated on substrates which have ordered grooves left from the first anodization (Fig.1.5A). This procedure produces domains of ordered pAAO that can be tuned through anodization conditions (Fig.1.5B).

The chemical reactions taking place during the anodization at the metal/oxide interface can be described as follows:

$$Al_{(met)} \longrightarrow Al^{3+}_{(ox)} + 3\,e^- \tag{1.21}$$

$$2\,Al^{3+}_{(ox)} + 3\,O^{2-}_{(el)} \longrightarrow Al_2O_3 \tag{1.22}$$

In eq.1.21 Al is oxidized to Al^{3+}, which then in eq.1.22 reacts with O^{2-} ions coming from water dissociation (eq.1.26) to form pAAO (Fig.1.6A).
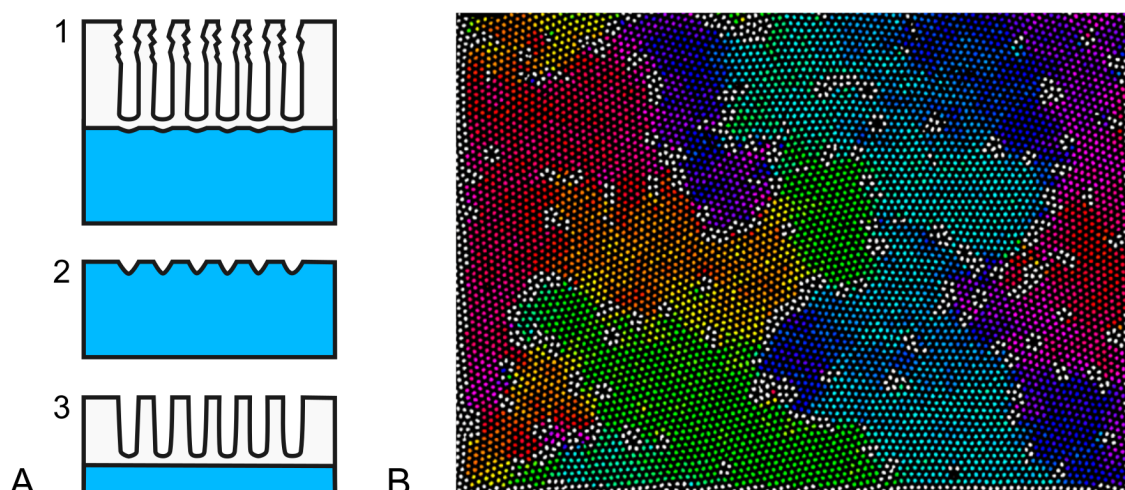
Figure 1.5: A - two-step anodization procedure with (1) first anodization resulting in disordered array of pores, (2) followed by dissolution of initial pAAO, (3) and second anodization which finally yields ordered pAAO structure; B - domains of uniformly oriented pAAO (highlighted), imaged by SEM. Figure adapted from [32].

Oxide/electrolyte interface reactions are listed below:

$$2\,Al^{3+}_{(ox)} + 3\,O^{2-}_{(el)} \longrightarrow Al_2O_3 \tag{1.23}$$

$$Al^{3+}_{(ox)} \longrightarrow Al^{3+}_{(aq)} \tag{1.24}$$

$$Al_2O_3 + 6\,H^{+}_{(aq)} \longrightarrow 2\,Al^{3+}_{(aq)} + 3\,H_2O_{(l)} \tag{1.25}$$

$$2\,H_2O_{(l)} \longrightarrow O^{2-}_{(ox)} + OH^{-}_{(ox)} + 3\,H^{+}_{(aq)} \tag{1.26}$$
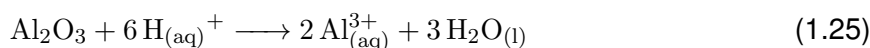
The reaction shown in eq.1.23 is identical to 1.22, with the only difference that it occurs at the oxide - electrolyte surface during pAAO anodization. In pAAO the growth occurs at the metal - oxide interface and any Al^{3+} present in the oxide is just ejected into the electrolyte (eq.1.24) (Fig.1.6A). In eq.1.25 the reaction responsible for the oxide dissociation due to Joule heating and/or field-induced effects is shown. Dissociation of water is shown in eq.1.26. This is the reaction that supplies O^{2-} ions to the formation of Al_2O_3 [32].

Close-packed hexagonal pAAO can be achieved only under carefully controlled conditions. Morphology of pAAO (Fig.1.6), like pore diameter (D_P), thickness (t), pore bottom radius (R), thickness of the barrier oxide (b), and interpore diameter (D_{INT}) can be tuned through j, concentration of the electrolyte, temperature, *etc.* Pores are usually surrounded by a volume of AAO with higher concentration of electrolyte ions that get incorporated into the oxide during the anodization (Fig.1.6C). This region is surrounded by ion-free native AAO that in certain cases also includes interstitial rods, the nature and origin of which are still up to a debate [36]. Highly uniform areas of pAAO ($>cm^2$) can be achieved with various imprinting or lithography methods
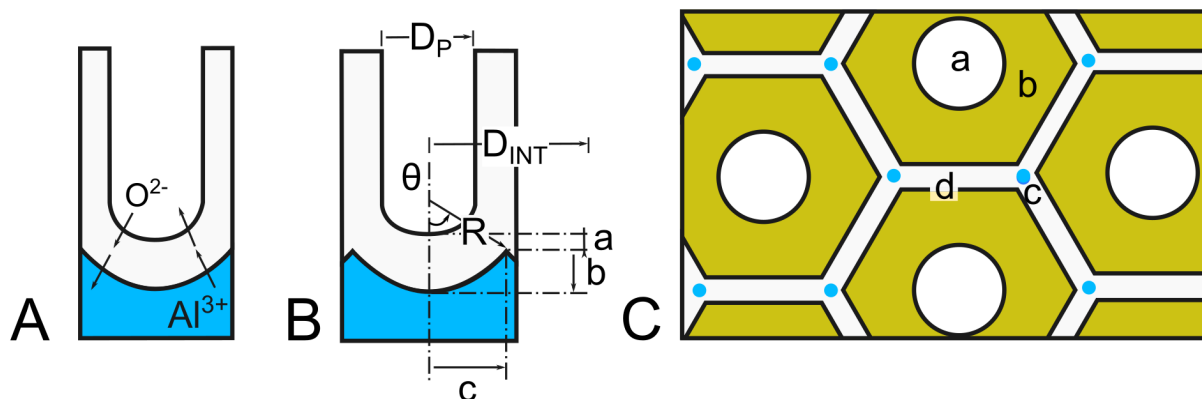
Figure 1.6: A - general outline of chemical reactions taking place during formation of pAAO. The most important is metal/oxide interface where Al from the bulk metal is transformed into Al_2O_3 with the help of O^{2-} coming from water dissociation at the oxide-electrolyte surface; B - most important geometrical features defining pAAO include D_P - pore diameter, D_{INT} - interpore distance, R - pore bottom radius, t - layer thickness, and b - barrier oxide thickness; C - outline and chemical composition of pAAO, top view: a - pore, b - AAO region with implanted electrolyte anions, c - interstitial rods, and d - pore walls. Figure adapted from [32].

and can produce not only circular pores but other shapes too [37].

Due to its highly regular structure, pAAO is an ideal template for creating new functional nanomaterials. Various approaches have been used to introduce a number of metals and semi-conductor materials inside the pores. Complex nanostructures like multisegmented nanowires made by electrochemical deposition (ECD) [38], ordered arrays of carbon nanotubes fabricated via chemical vapor deposition (CVD) [39], or single molecule DNA biosensors via atomic layer deposition (ALD) [40] are only a few examples that illustrate the versatility of pAAO applications. Ultra-thin freestanding pAAO has also been used as a stencil-mask for creating waveguides [41] or lasing devices [42] using a combination of deposition and etching techniques. Introduction of organosilane self-assembled monolayers (SAM) (e.g. APTES - 3-aminopropyl triethoxysilane) has been shown to be a convenient method to modify the pAAO surface due to -OH termination on its surface [43]. The pAAO surface can be also modified by different polymers for applications in gas separation, nanofiltration, protein adsorption, and catalysis [44]. The overwhelming number of applications denotes the relevance of pAAO to nanotechnology which will only grow in the future and will lead to more exciting discoveries.

1.4 Perovskites

Perovskites are a common class of crystalline structures known for their electronic properties and geological abundance. Gustav Rose was the first to discover perovskite $CaTiO_3$ in the XIX century and has named it after a Russian mineralogist Lev Alekseevich von Perovski. The majority of the naturally available perovskites are oxides, due to the fact that silicate perovskite, bridgmanite $((Mg, Fe)SiO_3$ and $CaSiO_3)$, makes up 93% of the lower Earth mantle [45]. Initially, the interest in perovskites was catalyzed by the discovery of high temperature superconductivity in cuprite oxide perovskites in 1987 [46]. Following it, more research was conducted on the synthetic oxide perovskites (OP), with some notable applications including capacitor dielectric materials $(BaTiO_3)$ and piezoelectric devices $(Pb[ZrxTi_1-x]O_3$ also known as PZT) [47]. Additionally, OP have been used for research in catalysis, colossal magnetoresistance, ferroelectrics, and multiferroelectrics [48].

The formal stoichiometry of perovskite is ABX_3, where A is metal/organic cation, B - metal cation, and X - oxygen/halide (Fig.1.7). Cubic structure (highest temperature phase) is the general motif for perovskites, although a variety of derivative structures exist due to geometrical alterations of constituent atoms or other external factors (tetragonal and orthorhombic phase, tilted octahedrons, *etc.*) [48], [47]. The unique perovskite 3D structure can be maintained only under certain combination of atom radii, governed by an empirical Goldschmidt Tolerance factor (α) [49]. The tolerance factor predicts that 3D perovskite structure can be preserved only when α falls between ~0.8-1.0, where α is defined in the following way

$$\alpha = \frac{r_A + r_B}{\sqrt{2}(r_A + r_X)} \tag{1.27}$$

More recently, perovskites came into research limelight due to an excellent performance of Pb containing halide perovskites (HP) in photovoltaic devices (PV) [50]. First investigation on HP was done as early as 1893 ($CsPbBr_3$) [51], but the structure was uniquely identified only in 1958 [52]. Groundbreaking success of $CH_3NH_3PbI_3$ ($MAPbI_3$) based solar cells could be attributed to the materials high charge-carrier mobilities, high diffusion length, and high absorption coefficient [53]. Subsequently, HP gained popularity in optoelectronics due to their simple synthesis, processability and strong photoluminescence (PL). Common HP ($CH_3NH_3PbX_3$, $CsPbX_3$, *etc.*) can be prepared by simple mixing of precursor solutions (CH_3NH_3X/CsX and PbX_2) and can be handled under ambient conditions with common solvents like n-dimethyl formamide (DMF), dimethyl sulfoxide (DMSO), and toluene. Nanocrystalline HP (ncHP) is
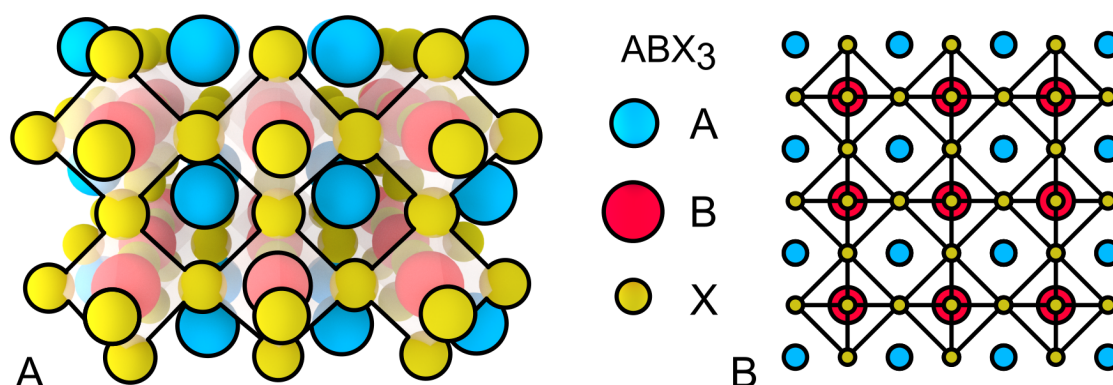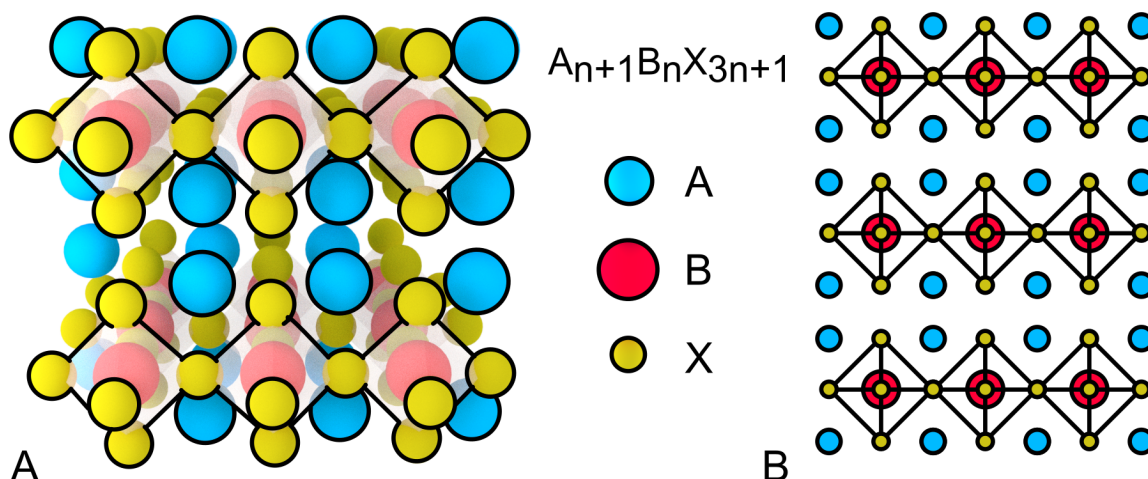
Figure 1.7: Schematic illustration of the classic perovskite ABX$_3$ structure in 3D (A) and 2D (B) projections. 3D halide perovskites are highly interesting for their use in photovoltaics and light emitting applications. In this illustration, blue spheres denote metal or organic cationw (A), red spheres are cation metal centers (B) and yellow spheres are anions (X), that can be either oxygen or a halide.

the most relevant material for light emitting applications, owing to its ease of color tunability through size control, narrow full width at half maximum (FWHM), and strong photoluminescence quantum yield (PLQY). ncHP can be synthesized in solution as a colloidal mixture or directly embedded into a polymer mixture or a porous matrix [54], [55], [56]. The fabrication of ncHP semiconductor layers is fast, low-cost, and reliable, while also compatible with other materials during thin film device fabrication [48]. A clear advantage of HP is its tolerance to different types of defects. HP were observed to have anion vacancies, which give rise to high ion mobility in the material [57], anion exchange effects [54], and high dynamic disorder [58]. Despite this and other defects that form at the grain boundaries and in bulk, HP optoelectronic properties remain unperturbed [48].

2D complex phases of perovskites are emerging as the next generation perovskite materials. The layered Ruddlesden-Popper structure ($A_{n+1}B_nX_{3n+1}$) is one of the available 2D perovskite superstructures that promises excellent electronic performance and has already been used to produce light emitting diodes (LED) [59] , [60], [61]. It also has a potential to be an alternative to environmentally hazardous 3D Pb-based perovskites [62], [63]. 1D perovskite structures are also available, but do not display appealing semiconductor properties (large band gap and poor electronic transport) [48].

Health hazard related to Pb based materials is a major obstacle on the way to the implementation of perovskite photovoltaic and optoelectronic devices on a large scale. Even though the active Pb containing part of a device is very small, the consequences of a prolonged exposure during production or use of a device are severe. Furthermore, HP quickly degrade

Figure 1.8: Schematic illustration of classic perovskite $A_{n+1}B_nX_{3n+1}$ structure in 3D (A) and 2D (B) projections; 2D halide perovskites are emerging perovskite group which can be used with alternative metal centers to avoid the effects of Pb toxicity. In this illustration blue spheres denote a metal or organic cations (A), red spheres are cation metal centers (B) and yellow spheres are anions (X), that can be either oxygen or a halide.

under ambient conditions to toxic compounds which have negative effects on humans and the environment [64]. The maximum allowed Pb content in human blood is 10 μg dL^{-1} (except children where no Pb exposure should be permitted, due strong influence on early development) [65], and 50 μg m^{-3} in air for work environment averaged for an 8-hour working day [66]. Presence of Pb in a human body can be localized to three compartments: (1) blood, (2) soft tissue, and (3) the skeletal system. Blood serves as a transfer route for Pb compounds, moving them to soft tissue, where they remain for short period of time after being deposited in the bones with a half-life of 20-30 years [64]. In the blood and soft tissue, Pb interacts with enzymes and various receptors mimicking Ca, Zn, and Fe metal centers. Deposition in the bones occurs in a form of lead phosphate. Even though unusual, high exposure acute symptoms are nausea, vomiting, abdominal pain, headaches, seizures, muscle weakness, and eventually death due to encephalopathy in a matter of days [66]. However, more common is a low long-term exposure to Pb through skin, respiratory tract or gastrointestinal system. It usually goes unnoticed and manifests itself later in life causing damage to blood, nervous, urinary, and reproductive systems often with lethal consequences [66]. One of the current approaches to deal with high toxicity of Pb in HP, is to replace it with Sn. Nevertheless, Sn-based perovskites and their degradation products are still soluble in water and remain considerably harmful [67]. Detrimental effects of Pb poisoning can be avoided by limiting exposure and applying appropriate protective measures. Nonetheless, currently very little control is done over perovskites

in research laboratories around the world.

2 Experimental

Materials

Table 2.1: Materials used during this master thesis.

Material	Formula	Supplier	Purity	Abbreviation
18 MΩ water	H_2O	TKA-Genpure	-	-
Acetone	C_3H_6O	VWR Chemicals	technical	-
Ammonium hydroxide	NH_4OH	VWR Chemicals	29%	-
Aluminum	Al	Chempur	99.999%	-
Cesium bromide	CsBr	AlfaAesar	99.998%	-
Copper chloride	$CuCl_2$	VWR Chemicals	99.998%	-
Dimethyl sulfoxide	C_2H_6OS	SigmaAldrich	>99%	DMSO
Dimethylformamide	C_3H_7NO	AlfaAesar	99.80%	DMF
Ethanol	C_2H_5OH	Merck KGaA	absolute for analysis	EtOH
Fluorine-doped tin oxide on glass	SnO_2-SnF_2	Xin-Yan Technlogy Ltd.	-	FTO
glass	SiO_2	Thermo Scientific	Pre-cleaned	-
Gold	Au	Ogussa	99.99%	-
Hellmanex	-	Hellma-Analytics	-	-
Hydrogen peroxide	H_2O_2	Chem-Lab	30% -	-

Table 2.2: Materials used during this master thesis cont.

Material	Formula	Supplier	Purity	Abbreviation
Hydrofluoric acid	HF	SigmaAldrich	48%	-
Hydrochloric acid	HCl	VWR Chemicals	37%	-
Isopropanol	C_4H_8O	VWR Chemicals	technical	IPA
Indium-doped tin oxide	In_2O_5Sn	-	-	ITO
Lead bromide	$PbBr_2$	SigmaAldrich	99.998%	-
Lead chloride	$PbCl_2$	AlfaAesar	99.998%	-
Lead iodide	PbI_2	AlfaAesar	99.998%	-
Methylammonium bromide	CH_3NH_3Br	GreatcellSolar	-	MABr
Methylammonium chloride	CH_3NH_3Cl	LIOS	-	MACl
Methylammonium iodide	CH_3NH_3I	GreatcellSolar	-	MAI
Molybdenum oxide	MoO_3	AlfaAesar	99.95%	-
Nitrogen stream	N_2	Linde	-	-
Oxalic acid	$C_2H_2O_4$	SigmaAldrich	99%	-
Phosphoric acid	H_3PO_4	AlfaAesar	85%	-
Platinum foil	Pt	-	-	-
Platinum wire	Pt	-	-	-

Table 2.3: Materials used during this master thesis cont.

Material	Formula	Supplier	Purity	Abbreviation
Silicon wafer	Si	Topsil	<100>, 1-10 Ω cm, thermal oxide	-
Silicon wafer	Si	Topsil	<100>, 1-100 Ω cm	-
Sulfuric acid	H_2SO_4	J. T. Baker	95-97%	-
Titanium	Ti	-	-	-

2.1 Quantum confined samples

2.1.1 Porous matrix preparation

pSi

Si wafers were cut with a diamond-tipped cutter into 1×1 inch squares and pre-clenead using the following washing steps: Hellmanex (2 v/v% aqueous), 2× DI (deionized) water, IPA, and acetone ultrasonication for 30 min each. Following pre-cleaning, the samples were cleaned using RCA (Radio Corporation of America) cleaning procedures [68]. RCA cleaning includes 2 steps: SC-1 (Standard Clean) and SC-2. SC-1 solution contains DI water, NH_4OH and H_2O_2 in volume ratio 5:1:1 and is used to remove mostly organic components. SC-2 solution contains DI water, HCl, and H_2O_2 in volume ratio 5:1:1 and is used to remove traces of metallic contaminants. Si wafers are cleaned for 30 min in each of the solutions at 80°C followed by a thorough rinsing with DI water after each of the steps. After the cleaning procedure was complete, a 100-200 nm Al back-contact was deposited on the non-polished part of the Si wafer sample, using physical vapor deposition (PVD) (1-5 nm s^{-1}, ~1×10^{-6} mbar). Afterwards, the samples were annealed at 300°C for 5 h inside of a N_2 filed glovebox in order to establish an ohmic contact. Following the contact deposition, Si wafer samples containing additional thermal oxide layer on their polished side, were treated with 1:10 EtOH diluted HF solution for about 1 min, in order to strip the aforementioned oxide layer. When cleaned completely, the silicon wafer samples were placed inside the Sailor cell (Fig.1.3), with an O-ring placed on top of it. During the electrochemical etching 1:1 HF:EtOH was used as an electrolyte, Pt wire as a cathode, and Al foil in order to reach the Al back contact. Si wafer samples were etched using Keithley 2400 SourceMeter for 20 min at room temperature under galvanostatic

conditions. A range of current densities was used to control the pore diameter. For the given doping levels of the Si wafers, pSi etching was only possible between 5-30 mA cm^{-2}. No pore formation was observed below 5 mA cm^{-2}, while above 30 mA cm^{-2} electropolishing was taking place, which resulted in pSi layer cracking and crumbling. After the etching, pSi samples were rinsed with absolute EtOH and treated with O_2 plasma at 50 W for 5 min (PlasmaEtch PE-25-JW), in order to change surface wetting properties of pSi and simultaneously quench the native pSi emission. Immediately after the plasma treatment, pSi samples were spin-coated with perovskite precursor solutions at 2400 rpm for 7 s, followed by 20 min heat treatment on a heating plate at 115°C in ambient atmosphere.

pAAO

1 mm thick microscope slide glass was cut into 1×1 inch squares and cleaned in the manner identical to Si wafer pre-cleaning procedure. For low temperature spectroscopy the samples were prepared on 1×1 cm squares of sapphire. After the cleaning, a layer of Ti (~30 nm, 0.1 nm s^{-1}) followed by a layer of Al (60-1000 nm, 1-5 nm s^{-1}) were deposited using PVD without breaking a vacuum (~1×10^{-6} mbar). The Ti/Al double layer was anodized in a solution of 0.2 M oxalic acid at room temperature at 5 V under potentiostatic conditions with a Pt foil as a cathode. Anodization was performed until the current started to quickly drop and the Ti/Al layer became partially transparent. In order to produce larger pores, Ti/Al layer was also anodized using phosphoric (0.3 M) and sulfuric acid (0.3 M) electrolytes (potentiostatic conditions, 0°C) yielding a range of pore sizes. After anodization, the samples were washed with DI water, dried under N_2 stream and treated with O_2 plasma for 5 min at 50 W. Immediately after plasma treatment the samples were spin-coated (2400 rpm, 7 s) with a perovskite precursor solution and annealed at 115°C for 20 min.

2.1.2   Perovskite preparation

3D perovskites

Precursor solutions were prepared by mixing appropriate components in DMF or DMSO. For preparation of MAPbCl$_3$, 280 mg of PbCl$_2$ and 76 mg of MACl were mixed in 500 µL DMSO and stirred at 60°C until the solution became clear. MAPbBr$_3$ was prepared by mixing 368 mg of PbBr$_2$ and 124 mg MABr in 1.10 mL of DMF and stirred overnight at 50°C, yielding clear colorless solution. CsPbBr$_3$ was prepared by mixing 367 mg of PbBr$_2$ and 215 mg of CsPb in 2.4 mL of DMSO and stirring overnight at 70°C, resulting in clear colorless solution. MAPbI$_3$

precursor solution was prepared by mixing 922 mg of PbI_2 with 334 mg of MAI in 2.25 mL of DMF and stirred until clear yellow solution formed. All the precursor solutions were filtered through polytetrafluoroethylene syringe filters (0.45 μm, Whatman) before spin-coating.

2D perovskite

$(MA)_2CuCl_4$ precursor solution was prepared by mixing 53.78 mg of $CuCl_2$ and 54.02 mg of MACl in 500 μL DMSO and filtered through polytetrafluoroethylene syringe filter (0.45 μm, Whatman). The precursor solution was drop-casted on a 1×1 cm glass that was pre-treated with O_2 plasma at 100 W for 5 min. Glass with the precursor solution was then annealed at $70°C$ for 1 h. Samples for SEM imaging were prepared on ITO covered glass in order to increase conductivity of the substrate. Single crystals of $(MA)_2CuCl_4$ were made by preparing saturated solution of $(MA)_2CuCl_4$ in EtOH and letting it slowly evaporate at room temperature for 3 days.

2.1.3   Light Emitting Diodes

Pre-patterned FTO on glass was thoroughly polished with a Al_2O_3/TiO_2 paste to decrease surface roughness. Subsequently, FTO patterned glass samples underwent the same cleaning procedure as pAAO and Si wafer samples (Hellmanex, DI, water, IPA, acetone). 30 nm of Ti ($\sim$0.1 nm s^{-1}) and 60 nm of Al ($\sim$0.2 nm s^{-1}) were deposited through PVD one after another without breaking the vacuum ($\sim1\times10^{-6}$ mbar). The double metal layer was then anodized in 0.2 M oxalic acid at 5 V, identical to the procedure described in pAAO preparation section. Upon anodization, a thin transparent layer of pAAO, on top of TiO_2 was formed. This sample was further treated with O_2 plasma for 5 min at 50 W to make the pAAO surface more hydrophylic for optimal perovskite precursor solution coverage. Perovskite precursor solution ($CsPbBr_3$ original precursor solution 1:22 diluted in DMF, $MAPbI_3$ original precursor solution diluted 1:15 in DMF) was spin-coated on the samples and the samples then were annealed at $115°C$ for 20 min. Afterwards, 0.5 wt% F8 (poly[9,9-dioctylfluorenyl-2,7-diyl] end capped with *N,N*-bis(4-methylphenyl)-aniline) dissolved in chlorobenzene was spin-coated on top of the structure at 3000 rpm until dry. Top contacts, MoO_3 (20 nm, $\sim$0.2 nm s^{-1}) and Ag (100 nm, $\sim$2 nm s^{-1}) were evaporated through a shadow mask using PVD ($\sim1\times10^{-6}$ mbar).

2.2 Material analysis

2.2.1 Photoluminescence measurements

PL spectra were measured with a Photon Technology International (PTI) spectrometer (QuantaMaster 40) equipped with double monochromators on the excitation and detection channel.

Time-resolved Photoluminescence

Bulk samples were measured on Spitlight Compact 100 yttrium-aluminum-garnet-Nd laser with emission at 355 nm (in case of Br containing systems) or 532 nm (for I containing system), with a pulse length ~10 ns and an energy of 50 µJ cm^{-2} in both cases. The spot size was measured to be 5 mm in diameter. Shamrock spectrometer SR-303i-A equipped with an intensified charge-coupled device camera (Andor iStar DH320T-18U-73 [gate step 2.5 ns, gate width 2.5 ns]) was used for the detection. The samples were under vacuum for the duration of the measurement. ncHP in pSi was measured in SSPD (superconducting single photon detector) Scontel Superconducting Nanotechnology in combination with PicHarp 300 by PicoQuant time-correlated single-photon counting system. SSPD system time resolution is ~300 ps. Excitation wavelength was 405 nm provided by pulsed diode laser with pulse duration ~1 ns (FWHM) at 1 MHz repition rate and pulse enrgy ~5 pJ. Excitation spot was focused with a microscope to 10 µm in diameter. Emission was collected with the same microscope objective and the photons were guided through a single-mode fiber to the SSPD. A long pass filter was used to stop the excitation before entering the fiber connected to the SSPD.

Photoluminescence Quantum Yield

Measurements were performed according to the previously described method [69] using pAAO on glass and bulk sample prepared on glass without pAAO with the same solution. All measurement were done on Photon Technology International spectrometer equipped with integrating sphere.

Photoluminescence stability

Similar to the previously described PL measurement, the samples were placed inside of PTI spectrometer and PL was measured in log scale time intervals over the period of ~28 h. Signal intensity was integrated after background subtraction. Signal peak position was also monitored over the duration of the measurement.

2.2.2 Microscopy

Optical microscopy

Measurements were performed on Nikon Eclipse LV100ND microscope for all of the samples.

Scanning Electron Microscope (SEM)

SEM measurements were performed on Zeiss 1540 XB CrossBeam SEM.

Transmission Electron Microscope (TEM)

TEM measurements were performed on JEOL JEM-2200FS TEM under STEM (Scanning Transmission Electron Microscope) mode operated at 200 kV and an Oxford SDD X-MaxB (80 mm^{-2}) EDX system. pSi samples were prepared through mechanical exfoliation from the porous area of the sample onto a holey carbon TEM grid. The pAAO specimens were prepared using focused ion beam (FIB) milling (1540 CrossBeam SEM, Zeiss). Before milling, a thin layer of gold was sputtered on the specimen. TEM lamellae were prepared using standard FIB cutting, lifting out, and transferring to a TEM grid, followed by a final thinning to about 100 nm with an ion energy of 5 keV to minimize preparation artifacts. STEM was performed in bright field and high angle annular dark field mode, that are sensitive to the z-contrast of the Pb-rich regions. Line and mapping analyses where carried out using EDX.

2.2.3 Electroluminescence measurement

Optical power output of LEDs was measured on Agilent B1500 parameter analyzer together with S2281, Hamamatsu calibrated Si photodiode.

2.2.4 X-ray Diffraction

XRD diffractogram of $(MA)_2CuCl_4$ was recorded using PANalytical X-Pert MPD system (λCuK_α = 1.5418 Å) in Bragg-Brentano configuration.

2.2.5 High-energy X-ray Diffraction

All the high energy X-Ray diffraction experiments were performed in Deutsches Elektronen Synchrtron facility in Hamburg.

Wide Angle X-ray Scattering (WAXS)

WAXS measurements were performed at high-energy P07 beamline at PETRA III at DESY. 30 mA cm^{-2} MAPI sample was measured with beam energy of 98.5 keV, focused to 5 μm × 50 μm at the sample using Al compound refractive lenses. The rest of the samples (15 and 25 mA cm^{-2}) were measured using beam energy of 80.0 keV and spot size 2 μm × 30 μm. The diffraction intensity was recorded using PerkinElmer XRD 1621 flat panel detector situated 2000 mm behind the sample. Reference pSi sample containing no ncHP was measured for both beam configurations. "Nika" package [70] for IgorPro from WaveMetrics and SASfit [71] were used to analyze the data.

Small Angle X-ray Scattering (SAXS)

SAXS measurements were performed at PETRA III P08 beamline at DESY (Deutsches Electronen Synchrtron). The samples were measured in transmission mode with the sample surface perpendicular to the X-ray beam (20.0 keV). PerkinElmer XRD 1621 flat panel detector was used to detect scattered intensity at a distance of 2440 mm behind the sample. The data was analyzed with the same software packages as in WAXS measurement.

2.2.6 Low Temperature Spectroscopy

All the samples were measured under vacuum at a range of temperatures in Oxford Instruments OptistatDry cryostat. Samples were excited at 405 nm for MAPbBr$_3$ and CsPbBr$_3$ and at 532 nm for MAPbI$_3$ samples using OBIS Coherent continuous wave lasers. The spot size was measured to be 5 mm in diameter. Shamrock spectrometer SR-303i-A equipped with an intensified charge coupled device camera (Andor iStar DH320T-18U-73) was used for the detection.

The signal evaluation was performed without peak fitting for all systems except of bulk MAPbI$_3$. Peak intensities correspond to signal maximum and peak energies/wavelengths correspond to the position of the signal maximum. FWHM was calculated by taking subtracting signal half maximum at lower energy from the value at higher energy. Due to the more complex nature of PL behavior in bulk MAPbI$_3$ sample, the signals were fitted with two Gaussian functions each and the required data was extracted form the fitting parameters.

3 Results

During this work a method of quantum dot (QD) synthesis inside porous oxide matrices was developed and investigated for producing ncHP. Four different systems were characterized, including organic-inorganic hybrid perovskites $MAPbCl_3$, $MAPbBr_3$, $MAPbI_3$, and fully inorganic $CsPbBr_3$ systems. The concept was realized in two nanoporous oxide platforms (pSi and pAAO) each of which show compelling properties and unique advantages. Through detailed structural analysis, the blue shift in PL of ncHP confined within nanoporous oxide platforms was correlated to the pore size and therefore the size of the crystals itself. Samples confined within pAAO were studied using low temperature spectroscopy. Furthermore, ncHP in pAAO were successfully incorporated into a working LED showing potential of this material for future solution-processed light emitting devices. An alternative Cu-based perovskite was investigated for its optical properties as potential replacement to toxic Pb-based perovskites.

SEM, TEM images as well as EDX analysis were done by Heiko Groiss and Günter Hesser from ZONA (Zentrum für Oberflächen- und Nanoanalytik), JKU. High energy X-ray analysis as well as data interpretation was performed by Janina Roemer, Anton Böhm, Bert Nickel from LMU Munich, and Uta Rütt, Florian Bertram from DESY (Deutsches Elektronen-Synchrotron) Photon Science. Thin film XRD analysis on Cu perovskites was performed by Cezarina Mardare from ICTAS (Institut für Chemische Technologie Anorganische Stoffe), JKU.

Part of this work has been published in [56].

3.1 Lead containing perovskites

3.1.1 Confinement in pSi

ncHP confined in pSi have been produced by allowing perovskite precursor solutions to crystallize within pSi matrix at high temperature. Due to the extremely small and highly tunable pore diameter of pSi, a considerable hypsochromic shift could be observed in ncHP when compared to the corresponding bulk PL emission (Fig.3.1). The largest blue shift observed in
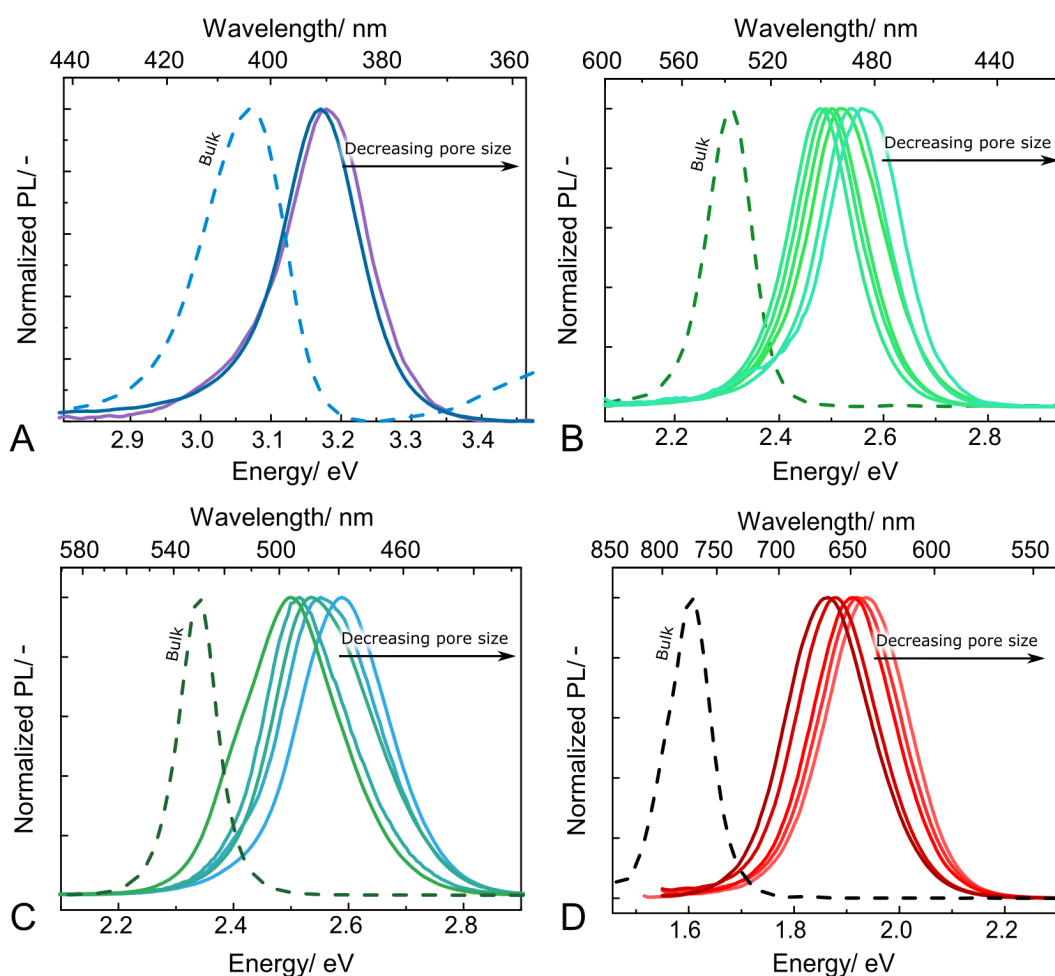
Figure 3.1: Comparison of bulk PL (dashed lines) and PL of perovskites confined within pSi (solid lines) in A - MAPbCl$_3$, B - MAPbBr$_3$, C - CsPbBr$_3$, D - MAPbI$_3$. Different degree of confinement and therefore different hypsochromic shifts can be achieved depending on the pore diameter in pSi. λ_{exc} = 350 nm for MAPbCl$_3$, λ_{exc} = 405 nm for MAPbBr$_3$ and CsPbBr$_3$, and λ_{exc} = 450 nm.

MAPbCl$_3$ system was 0.1 eV, in MAPbBr$_3$ 0.25 eV, in CsPbBr$_3$ 0.25 eV, and in MAPbI$_3$ 0.33 eV. These shifts, as well as the ability to control their magnitude, allowed for covering a significant portion of the visible spectra. In addition to high tunability, the confined PL showed narrow peak emission with an average of 0.14 eV FWHM in MAPbCl$_3$, 0.17 eV in MAPbBr$_3$, 0.20 eV in CsPbBr$_3$, and 0.18 eV in MAPbI$_3$. Similarly high performance has been achieved only in CdSe/CdS quantum dots, which require far more complex preparation procedures [72].

Precise control over the PL emission wavelength was achieved through adjustment of the pSi pore diameter and therefore the size of ncHP formed inside. The pore diameter was controlled via different current densities during pSi electrochemical preparation procedure and a clear linear relation could be observed between the pore size (current density used) and

peak emission energy (Fig.3.2). The degree of tunability heavily depends on the nature of the material, including its bulk band-gap energy and reduced exciton mass. Consequently, the large band-gap of $MAPbCl_3$ allows for only limited blue shift of the emission energy that is evident from the small difference between samples prepared in 10 and 25 mA cm^{-2} pSi. On the other hand, the small band-gap of $MAPbI_3$ permits strong blue-shift and excellent tunability.
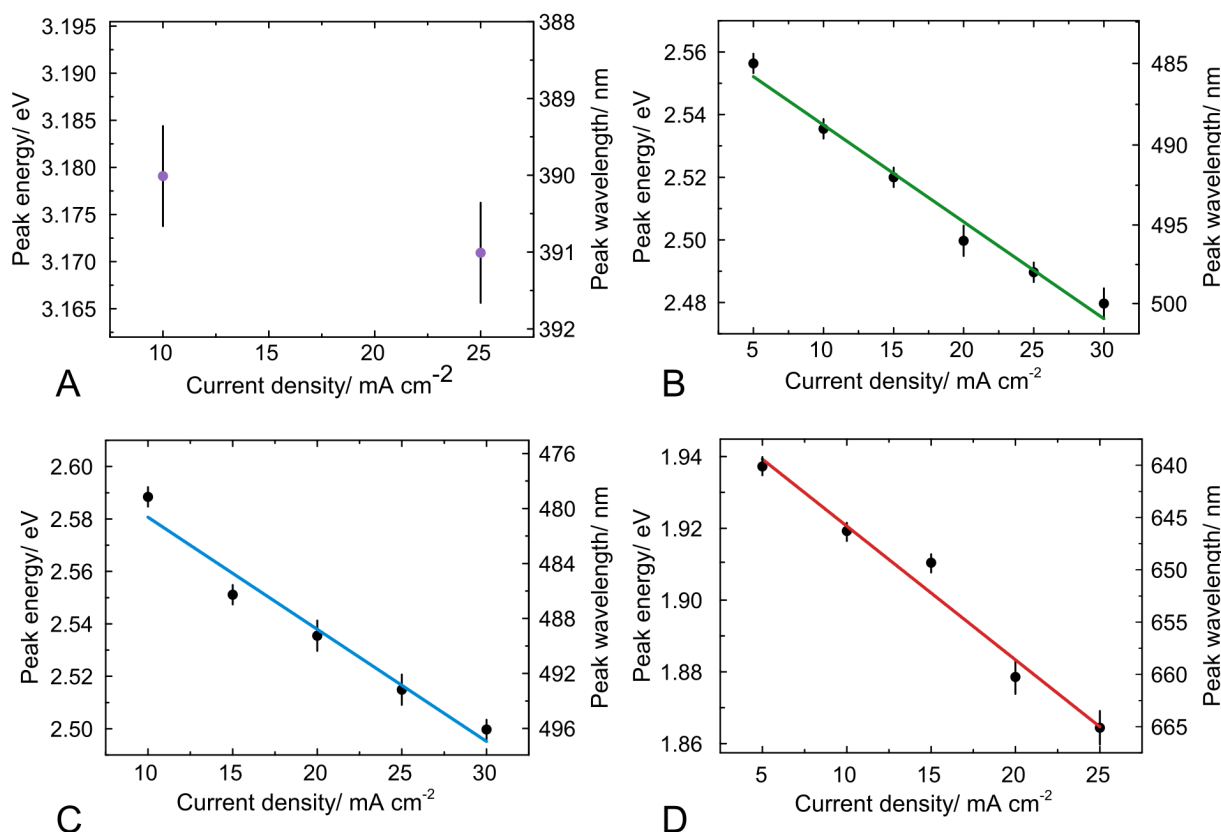
Figure 3.2: Dependence of PL peak position on current density during pSi preparation in A - $MAPbCl_3$, B - $MAPbBr_3$, C - $CsPbBr_3$, D - $MAPbI_3$. Smaller current density corresponds to smaller pore diameter, yielding a simple method to fine-tune materials emission.

Moreover, the ncHP confined in pSi display exceptionally bright PL, which could be easily observed with a naked eye under the illumination by an ordinary hand-held UV lamp (Fig.3.3). Homogeneous light emission over the area of square centimeters was easily achieved. Also the change in color associated with the PL shift could be easily observed. $MAPbI_3$, which usually emits in the infrared part of the spectrum, showed bright-red PL after confinement (Fig.3.3A). Normally green emission of $MAPbBr_3$ became blueshifted to cyan (Fig.3.3B) and the slightly different green bulk emission of $CsPbBr_3$ was shifted to blue (Fig.3.3C).

Changing the band gap of HP is possible not only through size dependent effects, but also by changing the halide anions and varying their ratios in a perovskite system. These two meth-
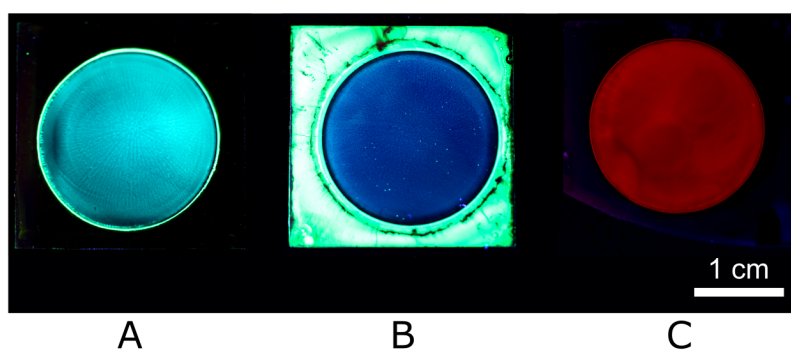
Figure 3.3: Bright luminescence observed from A - MAPbBr$_3$ B - CsPbI$_3$ C - MAPbI$_3$ confined within a pSi matrix; circular regions correspond to pSi that has been etched on a square piece of a planar Si wafer. Increased strength of the emission is evident in all the samples, since bulk emission is invisible to a naked eye in all cases but CsPbBr$_3$ where it is noticeably strong and different in color from the confined region. All samples illuminated with a hand-held UV lamp.

ods are not mutually exclusive, and to demonstrate this, MAPbI$_2$Br was prepared in pSi and its emission became blueshifted by 0.31 eV and the sample showed 0.08 eV FWHM (Fig.3.4). This allows to use confinement of ncHP within a pSi matrix to cover the majority of the visible spectra and to achieve precise tunability. It is important to add, that although spectral tunability can be achieved with mixed halide systems too, they tend to display unfavorable characteristics like appearance of new PL peaks upon light exposure, phase segregation, crystal disorder, and a notably large Stokes shift. Hence, single halide systems and precise control over their emission is the preferred way for future light emitting applications.
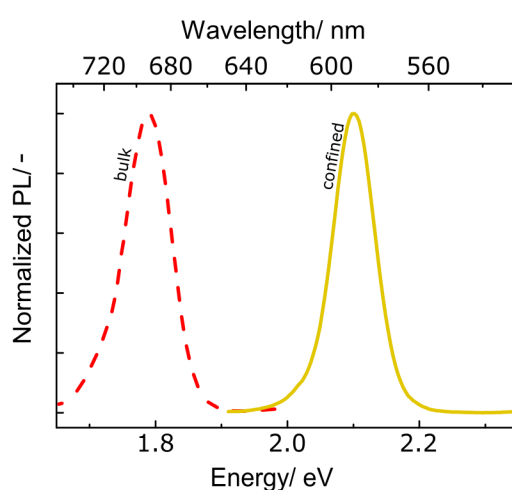
Figure 3.4: Comparison of bulk (dashed line) and confined (solid line) PL of MAPbI$_2$Br (prepared in 10 mA cm^{-2} pSi), showing that confinement in pSi works for both single and mixed halide systems. Excitation wavelength 450 nm.

Additionally, a time-resolved PL decay study was performed on ncHP in pSi (Fig.3.5). In all the cases the transient PL decay was fitted with a bi-exponential decay function resulting in short (τ_{SH}) and long (τ_{LO}) lifetime components. As it is seen in Fig.3.5, smaller particles (5 mA cm^{-2} etching conditions) show shorter radiative lifetimes (<1 ns) when compared to their larger counterparts (30 mA cm^{-2} etching conditions) (up to 7 ns). The corresponding bulk radiative life-time is significantly larger (up to 25 ns) and the results are summarized in Tab.3.1. Previously reported values for quantum confined particles radiative lifetime are in general agreement with values measured during this work [54], [73]. Higher quality bulk films have been reported to have radiative lifetimes up to several 100 ns [74]. The reason for decreasing lifetime in ncHP samples is the increasing recombination probability that results from a higher degree of overlap between electron and hole wavefunction that is typical for quantum confined particles [75], [76]. Other reports also partially contribute shorter lifetime to trap states originating in vacancies and substitutions in the ncHP structure [73].
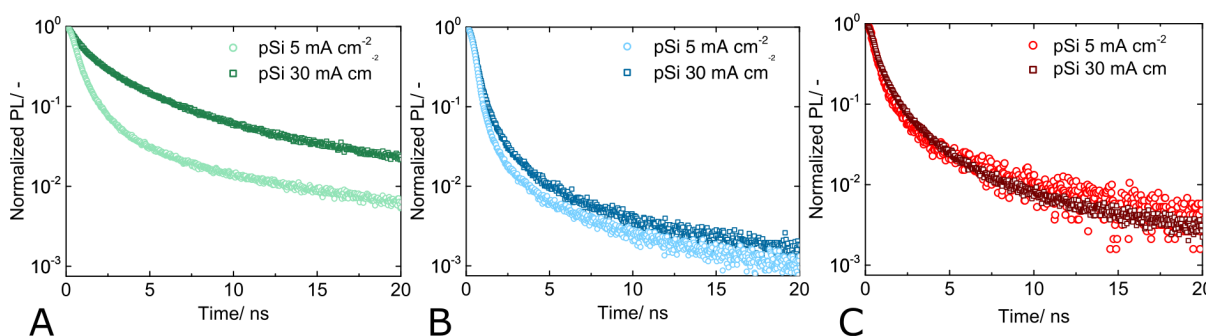
Figure 3.5: PL lifetime in pSi with *small* pores (5 mA cm^{-2}) and *big* pores (30 mA cm^{-2}). ncHP confined in pSi showed typical bi-exponential decay with smaller diameter pores having shorter time constants, when compared with pSi with larger pores (Tab.3.1). This behavior is typically observed in quantum confined particles [77].

3.1.2 Confinement in pAAO

pAAO was etched with an oxalic acid electrolyte under potentiostatic conditions out of Al metal thin films deposited on a glass substrate covered with a thin Ti layer. Several different electrolytes have been examined for pAAO etching including oxalic acid (0.2 M), sulphuric acid (0.3 M), and phosphoric acid (0.3 M) (Fig.3.6A). Oxalic acid was the easiest one to handle, since it can be used at room temperature and showed some of the smallest pores/highest degree of confinement when tested on MAPbBr$_3$ system. When infiltrated with perovskites, pAAO films showed blue-shifted luminescence (Fig.3.6B,C,D). A 0.07 eV hypsochromic shift was observed

Table 3.1: Time constants of PL lifetime experiment, as calculated from fitting a bi-exponential decay function to the measured data.

Material	Type	τ_{SH}/ns	τ_{LO}/ns
MAPbBr$_3$	5 mA cm^{-2}	0.31	1.24
	30 mA cm^{-2}	1.26	6.70
	bulk	3.70	8.30
CsPbBr$_3$	5 mA cm^{-2}	0.20	1.43
	30 mA cm^{-2}	0.23	2.14
	bulk	3.70	8.30
MAPbI$_3$	5 mA cm^{-2}	0.25	0.99
	30 mA cm^{-2}	0.32	1.03
	bulk	4.80	25.40

in MAPbBr$_3$, a 0.07 eV shift in CsPbBr$_3$ and a 0.1 eV shift in MAPbI$_3$ systems. Notably, the emission energy difference between bulk and confined ncHP is smaller when compared to its pSi counterparts, which can be attributed to the larger diameter of the pores in pAAO. FWHM of npHP appears to be larger in confined samples than in bulk samples. In MAPbBr$_3$ ncHP showed FWHM 0.12 eV vs 0.10 eV in bulk, CsPbBr$_3$ ncHP 0.10 eV vs bulk 0.09 eV, MAPbI$_3$ ncHP 0.15 eV vs bulk 0.08 eV. This phenomena has been previously reported in the literature and attributed to crystal distortions caused by the extremely small particle size [73].

Due to the transparent nature of thin pAAO films, it was possible to measure the absorption and therefore the optical band-gap of ncHP through the cut-off band edge via the Tauc plot method. Tauc plot usually consists of $h\nu$ - energy of light on the x-axis and a special value, $(\alpha h\nu)^{\frac{1}{r}}$, on the y-axis, where is α is absorption coefficient, and r a coefficient corresponding to the transition that occurs in the bandgap of the material [78]. In this case for all the systems a direct allowed transition was assumed, thus $r = \frac{1}{2}$. The band gaps of pAAO confined samples are larger when compared to their bulk counterparts, that is another indicator of quantum size effect. For example E_g(pAAO,MAPbBr$_3$) = 2.31 eV is larger than E_g(bulk, MAPbBr$_3$) = 2.28 eV and E_g(pAAO, CsPbBr3) = 2.37 eV is larger than E_g(bulk,CsPbBr3) = 2.31 eV. MAPbI$_3$ in pAAO displayed too small absorption coefficient to make a meaningful Tauc plot analysis (Fig.3.6D). Even though evident from the pronounced blue shift, the increased band gap could not be explicitly calculated for the MAPbI$_3$ system. pAAO MAPbCl$_3$ PL was too weak to detect, therefore the results are not included.

The PLQY of ncHP in pAAO was measured and it showed values significantly higher than
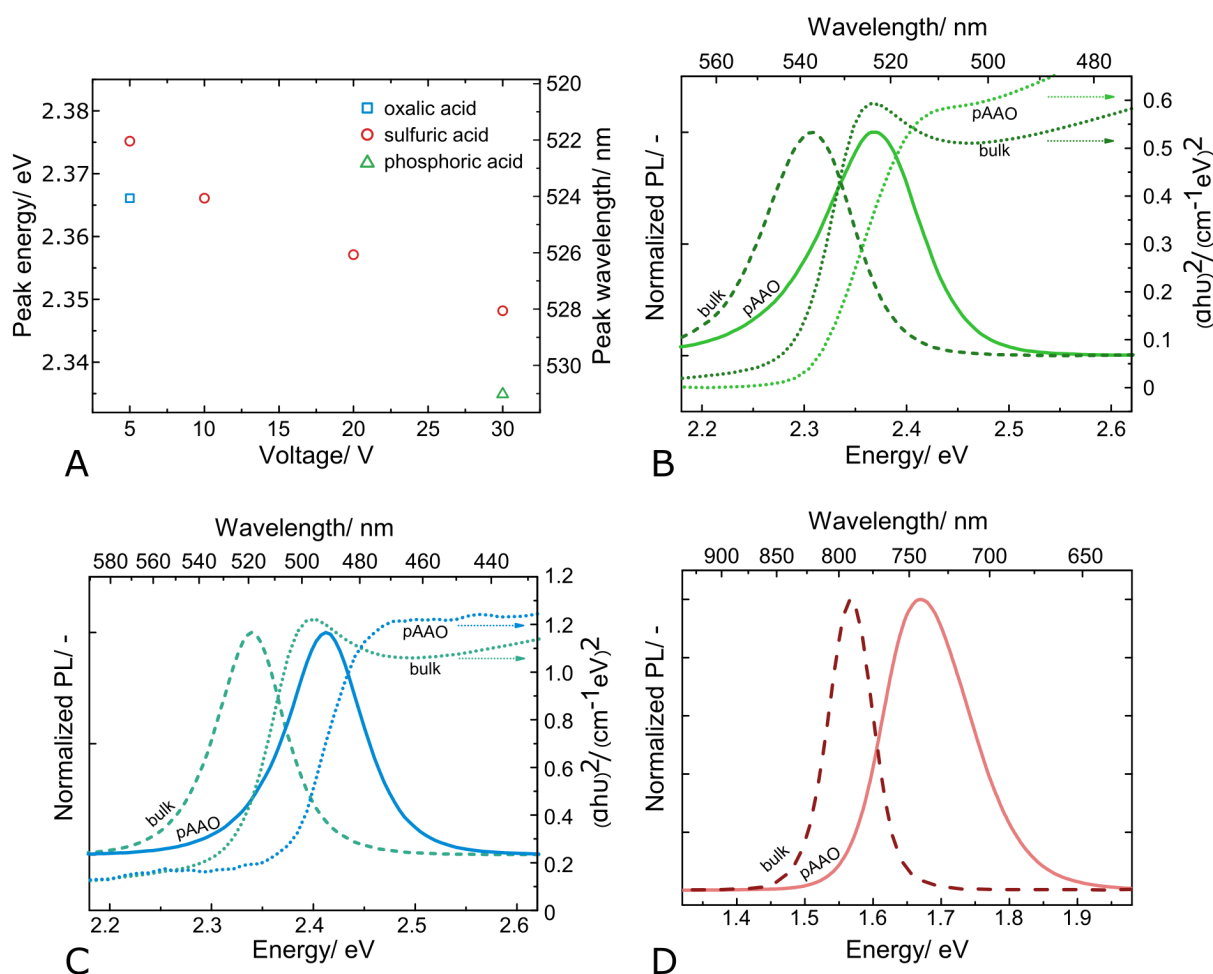
Figure 3.6: A - Peak PL of MAPbBr$_3$ confined in pAAO etched in various electrolytes at different voltages; PL of B - MAPbBr$_3$, C - CsPbBr$_3$ and D - MAPbI$_3$ bulk (dashed line) on glass and confined within pAAO (solid line) together with corresponding Tauc plot absorption data (doted line) showing pronounced blue shift in all of the cases. Tauc plot absorption data for MAPbI$_3$ confined in pAAO is unavailable due to its low absorption. MAPbBr$_3$ and CsPbBr$_3$ λ_{exc} = 405 nm. MAPbI$_3$ λ_{exc} = 450 nm.

those found in their bulk counterparts. pAAO confined MAPbBr$_3$ showed a PLQY of up to 60% ($\overline{x}$=36.04%, σ=16.23%, n = 4), CsPbBr$_3$ up to 90% ($\overline{x}$=54.84%, σ=31.98%, n = 4), and MAPbI$_3$ up to 25% ($\overline{x}$=13.76%, σ=9.17%, n = 4). Bulk samples on average showed a PLQY between 1 and 2%, which compares well with the values reported in the literature [54].

Thin films of aluminum oxide (~200 nm) containing ncHP on glass substrate showed bright PL over a large area which could be easily observed with a naked eye under a UV lamp illumination (Fig.3.7).

As well as in pSi, a mixed halide system was introduced inside the pAAO to proof the breadth of applicability of the method. MAPbBr$_2$Cl was confined in pAAO and also shows blue
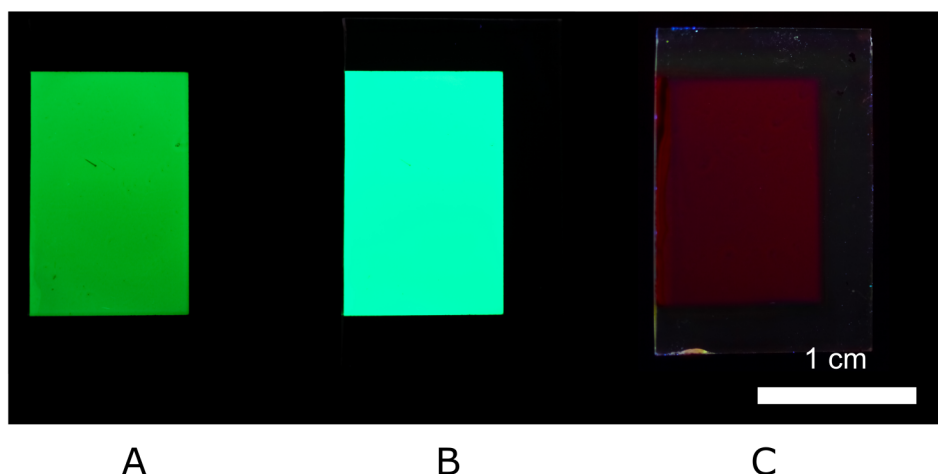
Figure 3.7: Bright luminescence over large area of A - MAPbBr$_3$, B - CsPbBr$_3$, C - MAPbI$_3$ confined in pAAO visble to a naked eye under a UV hand-held lamp.

shift when compared to the bulk PL emission (ΔE = 0.13 eV, confined FWHM = 0.15 eV, bulk FWHM = 0.11 eV). This system also suffered form phase separation and relatively low stability under ambient conditions.

Another distinct property of pAAO matrix is its encapsulation ability. When comparing PL intensity over time of MAPbBr$_3$ and CsPbBr$_3$ (Fig.3.9A,C respectively) one can observe significantly better results when compared to bulk films, which tend to quickly decay. Surprisingly, ncHP in pAAO increase their PL intensity over time, CsPbBr$_3$ by up to 40% and MAPbBr$_3$ by up to 20%, then going back to their original values. This unusual behavior has been re-
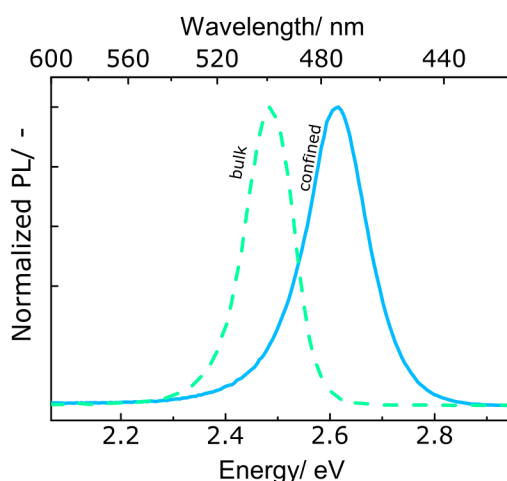
Figure 3.8: Proof-of-concept illustration of MAPbBr$_2$Cl confinement within pAAO, showing that the method is also applicable for the mixed halide system; confined PL (solid line) shows hypsochromic shift compared to bulk PL (dashed line); λ_{exc} = 405 nm.
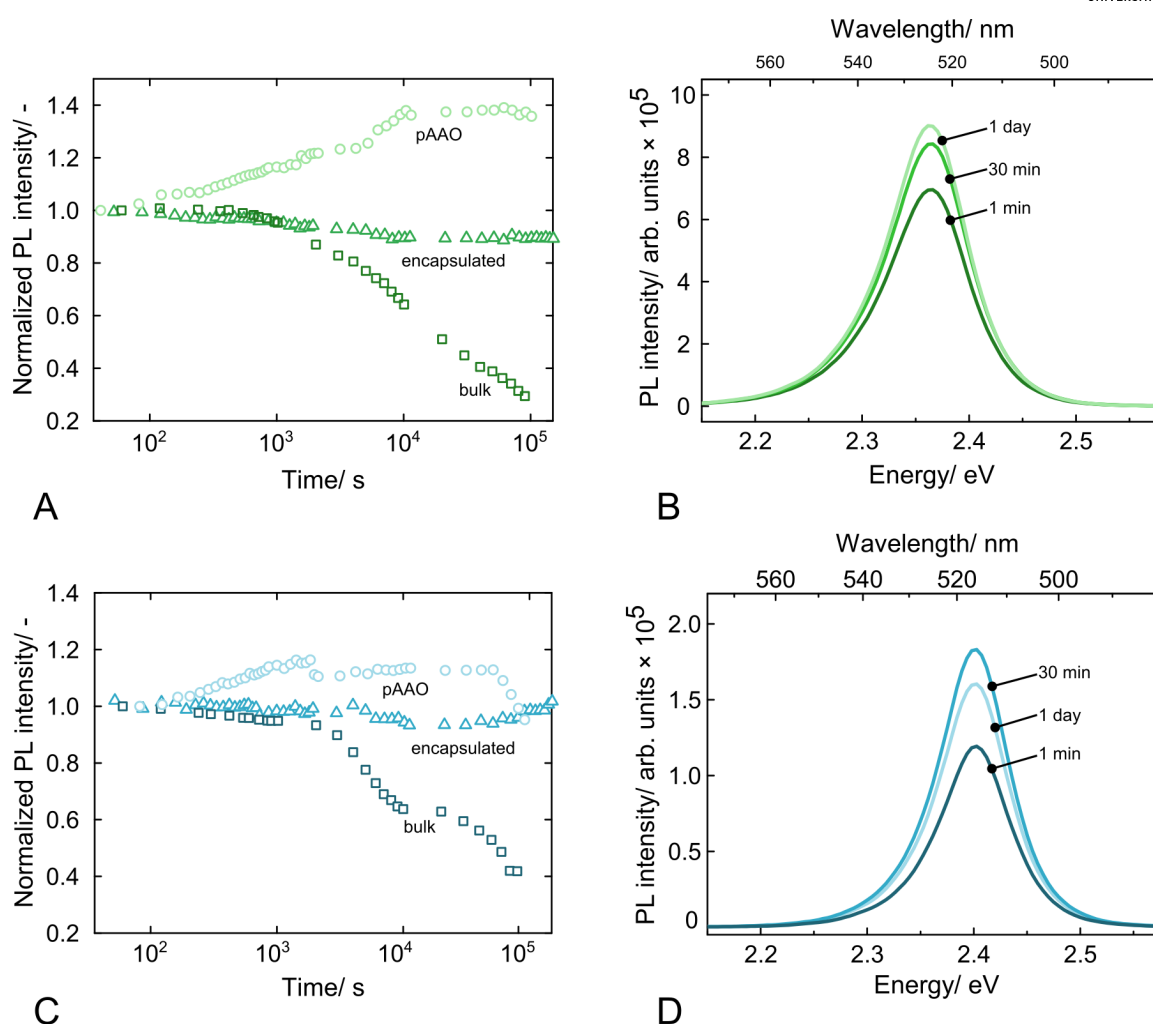
Figure 3.9: A - integrated PL intensity of MAPbBr$_3$ as a function of time for bulk MAPbBr$_3$ (squares), MAPbBr$_3$ confined within pAAO (triangles) with encapsulation and without encapsulation (circles); B - PL spectra showing the constant position of PL peak after 1 min, 30 min and 1 day; λ_{exc} = 405 nm.

ported previously in the literature and has been ascribed to influences of the environmental conditions [79]. Some of the studies report clear correlation of the photophysical response to the presence of H$_2$O and O$_2$ as well as full reversibility of the PL enhancement [80]. In this case the phenomenon was attributed to physisorption of certain gases on the surface of the crystal. Other publications attributed the PL enhancement to reaction of O$_2$ with trapping sites and their subsequent deactivation [81]. On the other hand, in another study oxygen has been reported to have a limited role in this process [82]. Evidently, the topic is still a matter of a debate and shall be investigated further. In this work, presence of ambient atmosphere (moisture and oxygen) seem to play an important role, since when the samples were encapsulated with epoxy and glass slides, PL intensity remained constant over time. Furthermore, PL spectra

of the samples was examined and no apparent shifts or appearance of additional peaks were observed (Fig.3.9B,D).
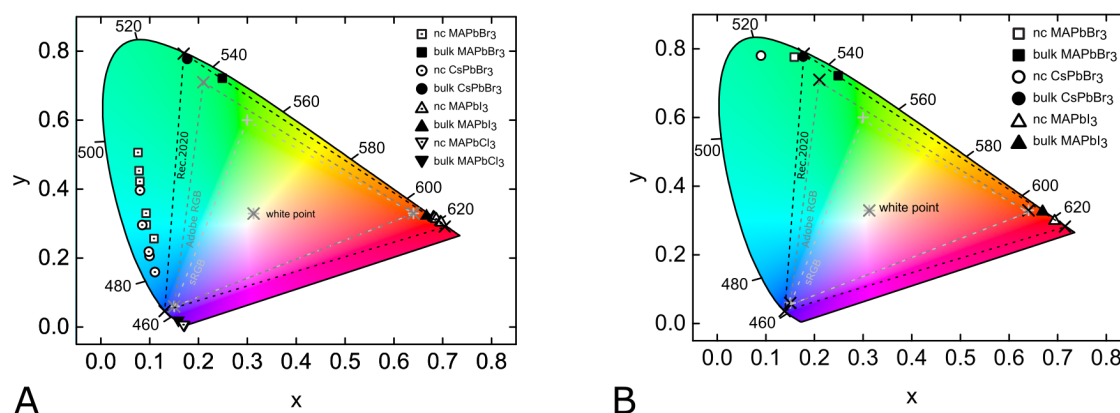
Figure 3.10: Emission of ncHP confined in A - pSi and B - pAAO summarized in CIE 1931 color space diagram, showing that color purity of both pSi and pAAO samples extends beyond the existing standard color spaces (sRGB and Adobe RGB).

The CIE (Commision Internationale de l'Eclairage) chromaticity diagram allows to compare light emitting properties of different electronic devices and compare them to each other. Over the years various recommendations have been issued by different groups and companies defining **r**ed, **g**reen and **b**lue colors in order to smoothen the additive color mixing workflow in display and cinema industry. All of them aim to cover the so-called Pointer's space, the gamut of real surface colors as they are perceived by an average human eye. Some of the standards include sRGB and Adobe RGB which are often used in TV, computer science and software development. The most modern standard is Rec.2020 (that covers 99.9% Pointer's gamut) and it aims to set a standard for ultra high definition TVs. QD based TV screens have been reported to be the most likely to fully meet Rec.2020 [83]. Fig.3.10 shows how the PL of the samples prepared during this work compare to industry issued standards. The emission of pSi samples (3.10A) almost in all cases lies beyond the industry standards. While greens and cyans of $MAPbBr_3$ and $CsPbBr_3$ are located far away from standard green and blue points, $MAPbCl_4$ and $MAPbI_3$ show deeper blue and red colors respectively. Out of the available pAAO samples (3.10B), $CsPbBr_3$ shows the most attractive properties, because it goes far into the green region. pSi samples, with the right approach, could potentially be used as phosphors in LEDs to expand the existing color gamut and its purity. pAAO samples can also be incorporated directly into LED device architecture.

3.1.3 Structural analysis

In-depth structural analysis was performed in order to confirm that the hypsochromic PL shift is caused by quantum confinement size effects. In Fig.3.11 a representative SEM image of a pAAO surface etched in 0.2 M oxalic acid is shown. The image shows randomly distributed pores all <10 nm in size, which allows to make a first estimate of the pore size in pAAO and therefore crystal size of perovskites that are embedded in it. Sample porosity was estimated to be ~15% from image analysis of SEM data using ImageJ software [84].
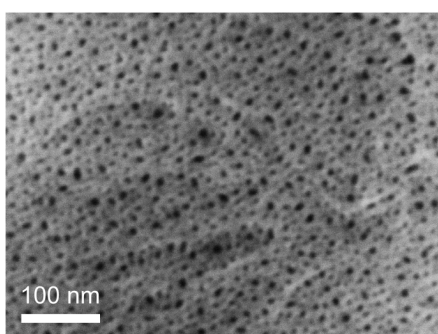
Figure 3.11: SEM image of pAAO etched in 0.2 M oxalic acid at 5 V, top view, nanometer-size porous structure of the porous oxide matrix.

TEM was used to image nanocrystalline $MAPbI_3$ encapsulated in pSi and also in pAAO. The BF-STEM image in Fig.3.12A shows an exfoliated flake of pSi, that appears gray, with dark spots of nanocrystalline $MAPbI_3$ implanted in it. The nanocrystals appear larger and darker to the right side of the image due to the increased thickness of the pSi piece under investigation. In Fig.3.12B a cross section of pAAO prepared by FIB milling, half-filled with ncHP is shown. An unordered network of pores all oriented perpendicular to the substrate is visible as well as perovskite nanocrystals embedded in it. Based on previous studies and available SEM and TEM images of the porous oxide material, a 3D render was made to visualize the structures (Fig.3.12C,D) [6], [32].

Additionally, a pSi sample was analyzed with high-angle annular dark field (HAADF) STEM and EDX was used to confirm that the embedded particles were indeed Pb containing perovskite. Performing a line scan though a perovskite particle (Pb L line), it was also possible to measure the particle diameter to be ~4 nm.

To further investigate crystallite size (also pore size and their relation to current density used during anodization to achieve a given pore size), high energy X-Ray diffraction studies were performed on three samples of pSi etched under different conditions (15, 25, 30 mA cm^{-2} with
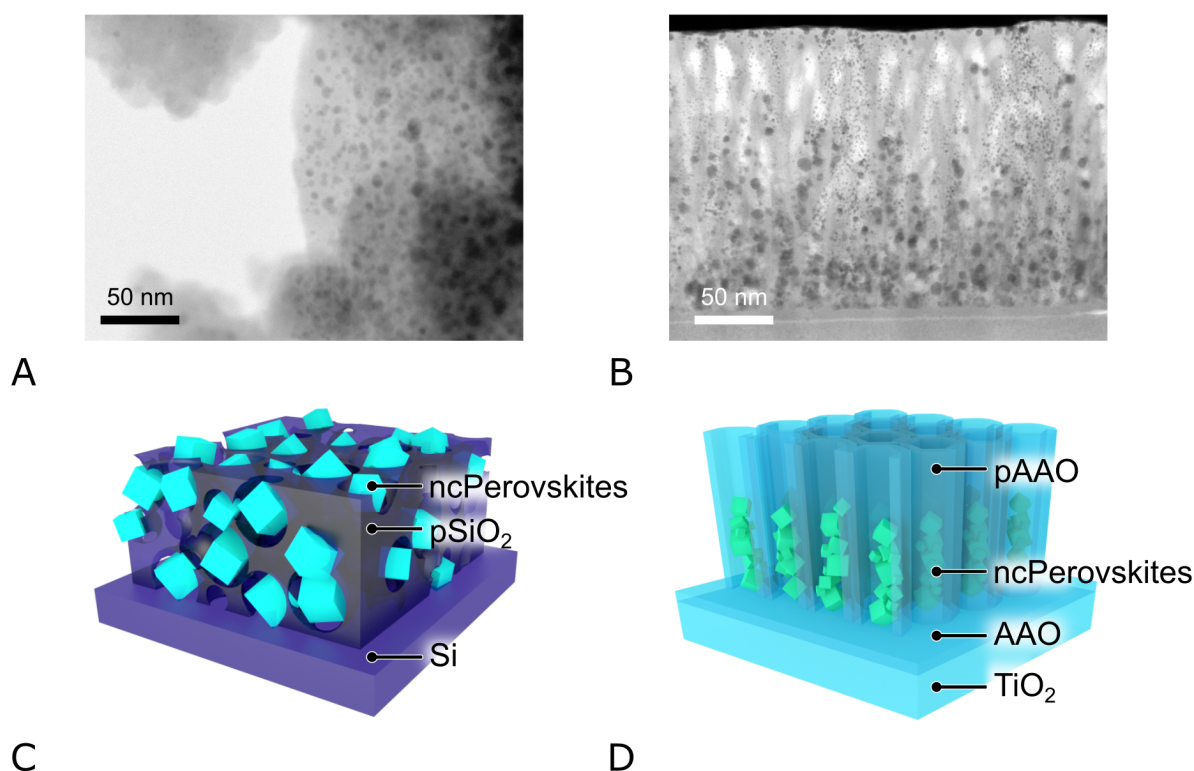
Figure 3.12: A - BF-TEM image of MAPbI$_3$ nanocrystals (dark inclusions) in exfoliated 15 mA cm^{-2} pSi (gray) sample; B - BF-TEM image of ~100 nm thick slice of pAAO half-filled with MAPbI$_3$ nanocrystals (dark inclusion); C - illustration of interconnected pSi matrix with perovskite nanocrystals embedded in it; D - illustration of pAAO vertically aligned oxide matrix filled with perovskite nanocrystals.

MAPbI$_3$ embedded in it). X-Ray scattering analysis can be categorized as reciprocal space technique, wheres SEM and TEM are real space techniques. Even though both techniques aim to probe and analyze electron density of the samples, X-Ray scattering is not limited in terms of analysis area and it is non-destructive. Furthermore, a typical tendency of sample bias in TEM or SEM is eliminated since the signal is averaged over a macroscopic sample volume [85]. The main advantage of using high energy X-rays obtained from an accelerator is its high brilliance beam. High brilliance is a term describing number of photons produced per second, angular divergence, cross-sectional area of the beam, and the number of photons falling within 0.1% of bandwidth of the central wavelength [86]. Brilliance achieved at the synchrotron facilities is usually many orders of magnitude larger than brilliance of regular lab X-Ray sources, thus allowing investigation of sub-nanometer structures with extremely high precision.

In the case of pSi, a high energy microfocus beam was used to scan the sample on its surface (Fig.3.14B) and at a number of points inside the sample to obtain a depth profile
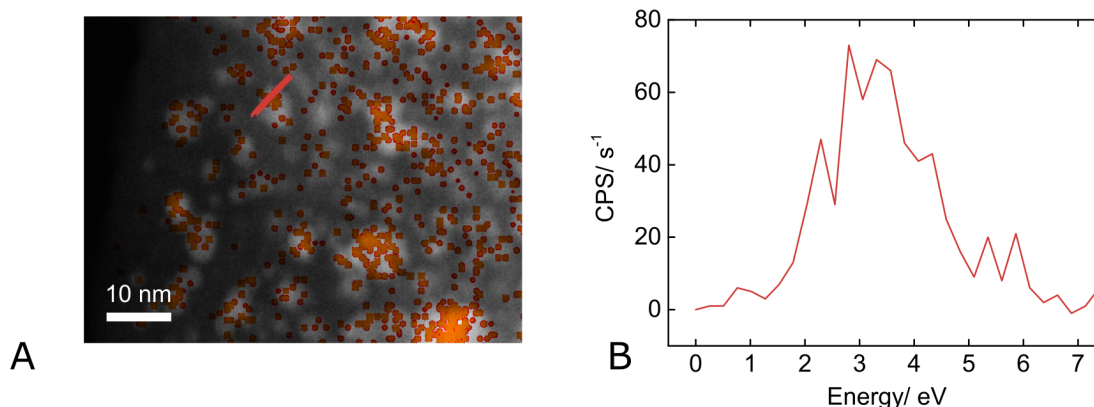
Figure 3.13: A - EDX analysis of 15 mA cm^{-2} pSi flake filled with MAPbI$_3$ (light inclusions); orange points indicate Pb containing areas of the image and red line indicates the scan line; B - EDX scan line analysis (Pb L line) showing the size of the ncMAPbI$_3$ crystals to be *ca.* 4 nm.

(Fig.3.14B). Empty pSi matrix was scanned (Fig.3.14C,D) in order to acquire a background signal and used to correct the azimuthally averaged signal that was plotted as a function of the scattering vector **q**. When the pSi sample containing perovskites was studied, the resulting diffractograms calculated from Debye rings could be assigned to a tetragonal MAPbI$_3$ structure. Lattice constants calculated from the data (a=b=8.90(3) Å, c = 12.71(5) Å) compare well with those reported previously in the literature [87]. Broadening of the diffraction peaks can be correlated to the size of the crystals through a Scherrer equation (eq.3.1)

$$\tau = \frac{K\lambda}{\beta \cos(\theta)} \qquad (3.1)$$

where τ - mean size of the crystallites, K - dimensionless shape factor, λ - wavelength of the incident X-Ray beam, β - line broadening at FWHM, and θ - is the Bragg angle. When plotted together, it is easy to see the broadening of the diffractogram signal in the samples with smaller pore size, signifying a size decrease of the ncHP crystals formed in there (Fig.3.14E).

The depth profile of each of the three differently sized samples was analyzed in detail in order to assess crystalline size distribution and the amount of perovskites accumulated at a certain level in the depth profile (diffraction power) (Fig.3.15A,B,C). It is found that in each of the pSi samples a relatively uniform crystal size distribution is obtained throughout the depth of the sample. Average values for samples prepared with 15, 25, and 30 mA cm^{-2} have been calculated to be 1.8, 2.1, and 4.5 nm respectively. For a semiconductor nanocrystal to show size-dependent quantum effects, the diameter of the particle must be similar or smaller than the natural delocalization lengths of an exciton in a bulk semiconductor (exciton Bohr diameter, a_0). This values have been previously reported in the literature [a_0(MAPbBr$_3$) = 2.2 nm [88]]
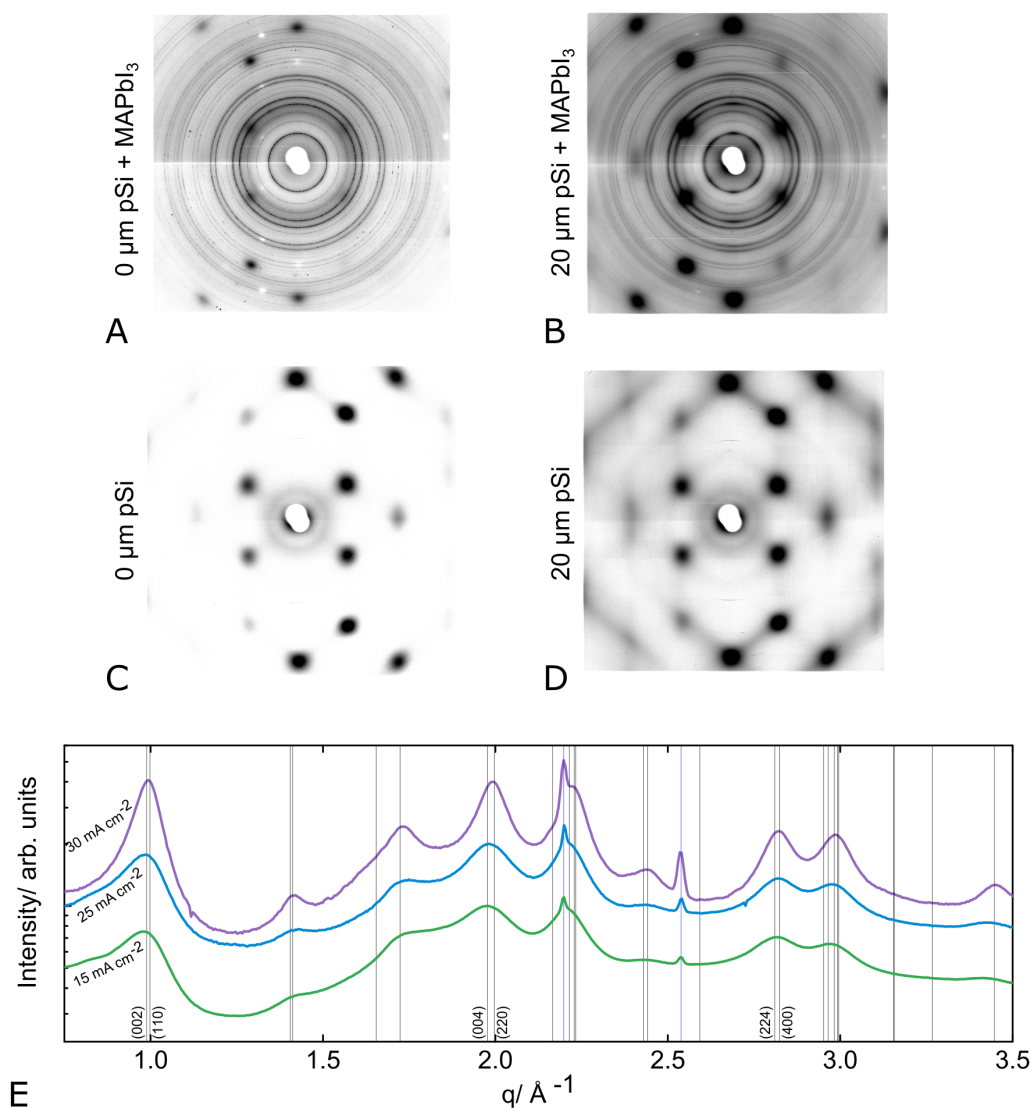
Figure 3.14: Examples of WAXS measurement results of 15 mA cm^{-2} pSi with MAPbI$_3$ embedded in it A - on the surface and B - 20 μm deep underneath the surface; both sets of results show a dot pattern resulting from crystalline silicon and circular patterns resulting from MAPbI$_3$; as a negative control a sample of empty pSi was also scanned C - on the surface and D - 20 μm underneath the surface showing only silicon patterns; E - diffractogram showing peaks corresponding to crystallites of MAPbI$_3$ embedded in a matrix of pSi etched at different current densities, therefore having various pore sizes.

and when compared to the crystallite size of MAPbI$_3$ in pSi as inferred from the high energy X-Ray diffraction study, strongly suggests quantum confinement effects as the reason for the band-gap change (Fig.3.15D).
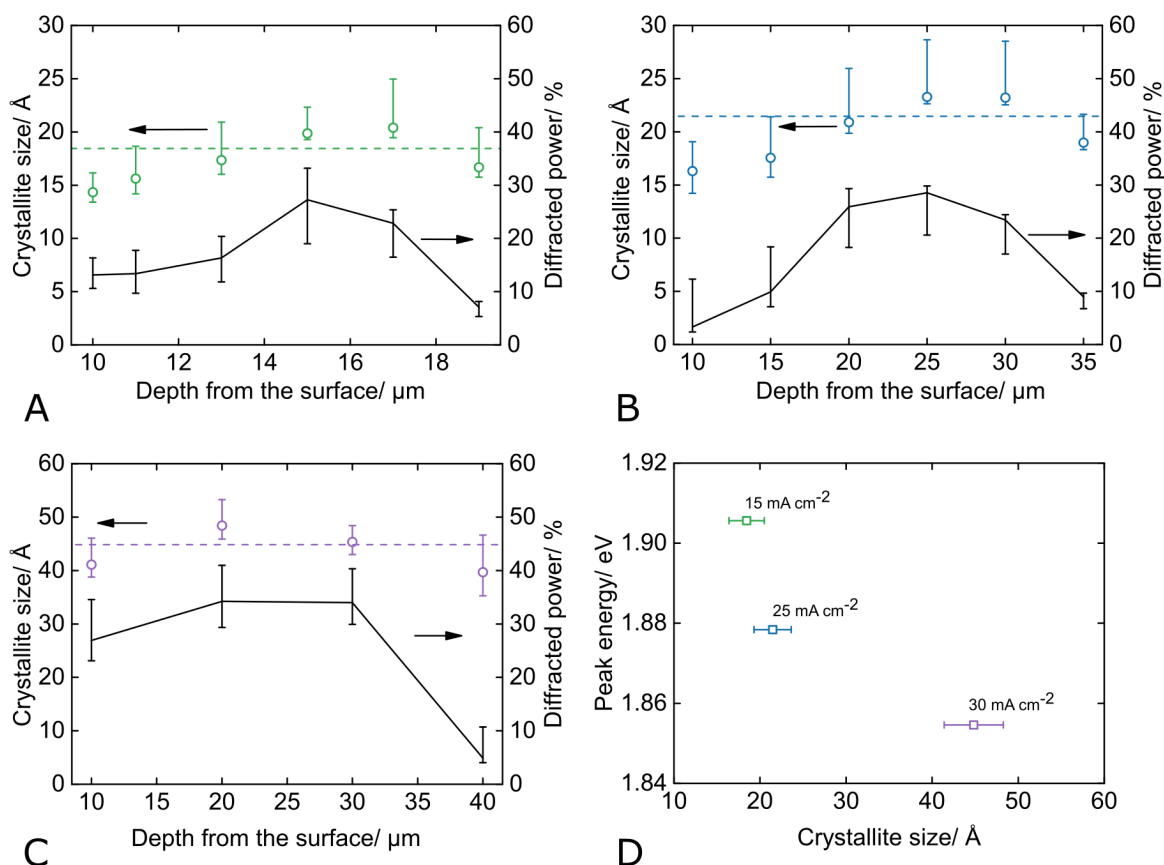
Figure 3.15: Based on the Scherrer analysis of MAPbI$_3$ embedded into pSi matrix, the crystallite size could be resolved as a function of matrix depth; nanocrystallites prepared in pSi etched at A - 15 mA cm^{-2}, B - 25 mA cm^{-2}, C - 30 mA cm^{-2} were analyzed; D - average PL peak positions plotted as a function of crystalline size.

Small angle X-Ray Scattering (SAXS) was used to study the porosity and pore size of pSi matrices. The data collected at small angles (between 0.1-10 degrees) contains valuable information about the electron density at nanometer length scales. A specific advantage of SAXS measurement is the ease of nanoporous material analysis. Since the technique measures electron density differences, pores can be regarded as the inverse particles, therefore allowing the use of existing theories and principles for full examination of the structures [85]. In the following experiment, a 15 mA cm^{-2} pSi sample without perovskites was analyzed to further investigate the properties of the matrix. The transmission signal collected at the 2D detector shows the angle-resolved signal that is elastically scattered from the pSi sample (Fig.3.16A). The data is further reduced from its 2D form to the corresponding 1D form by plotting the

azimuthally averaged intensity signal vs. the scattering vector **q** (Fig.3.16B), the modulus of which is defined by the following formula (eq.3.2):

$$q = \frac{4\pi \sin(\theta)}{\lambda} \tag{3.2}$$

where θ - scattering angle, and λ - radiation wavelength. The Porod invariant Q could be calculated from the given data by numerically integrating the scattering curve ($Q = \int_0^\infty q^2 I(q) dq$). Using the Porod representation of the data in the form of I(q) q^4 vs. q, it is possible to extract the constant K by extrapolating from a plateau formed between 0.15-0.25 Å^{-1} (Fig.3.16C). K is proportional to the surface area of all the pores in the path of the beam [89]. Finally, the porosity of a pSi sample could be calculated using formula (3.3) [90]:

$$\Phi = 1 - \frac{lnT_{npSi}}{lnT_{Si}} = 57\% \tag{3.3}$$

where Φ - porosity, T_{npSi} - transmission of the porous layer, and T_{Si} - transmission of the bulk silicon. Using the obtained Porod invariant Q, constant K and porosity Φ, it is possible to calculate an estimate of the pore diameter (d) using the following formula (eq.3.4) [90]:

$$d = \frac{4}{\pi(1 - \Phi)} \frac{Q}{K} = 4.0 \quad nm \tag{3.4}$$
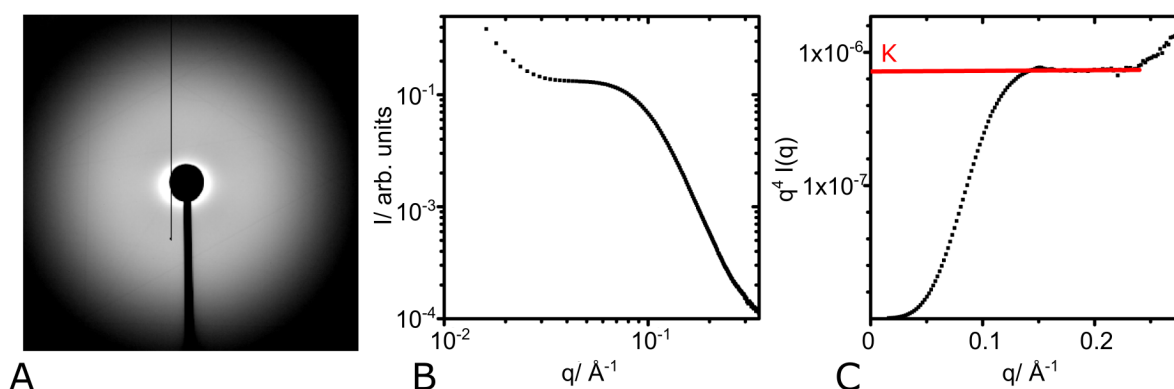
Figure 3.16: SAXS measurement performed on a 15 mA cm^{-2} pSi sample; A - transmission data obtained from the sample positioned perpendicular to the incident beam; the shape in the middle is the beam stop shadow; B - reduced and background substracted intensity data plotted as a function of scattering vector **q** (3.2); C - Porod representation of the same data set, allowing to extract the Porod constant K that is used to determine the pore diameter.
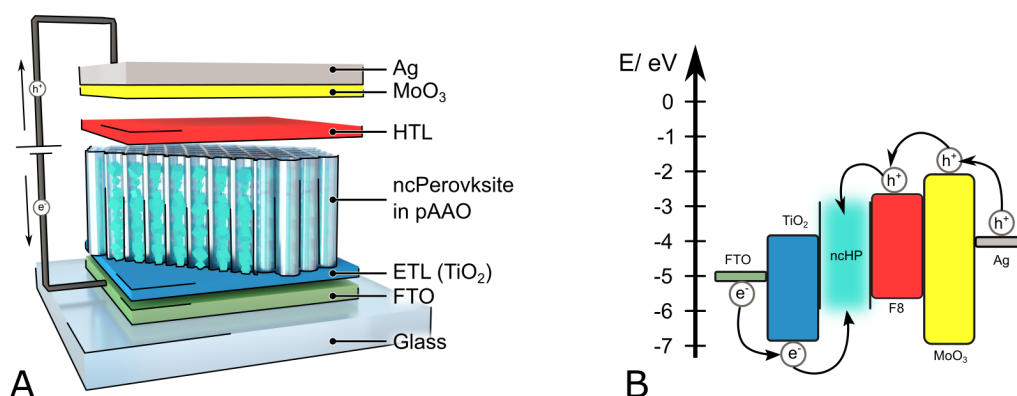
Figure 3.17: A - Device structure of an LED incorporating ncHP within a porous oxide matrix; the LED was prepared by evaporating Al/Ti thin films on a FTO transparent electrode resulting in a pAAO that was further infiltrated with perovskite precursor solution; the compact TiO_2 layer that resulted from anodization serves as a electron transporting layer (ETL) and F8 conducting polymer was spincoated on top of the structure to serve as a hole transporting layer (HTL); Ag/MoO_3 was used as top contacts for this LED; B - energy level diagram of the LED; ncHP confined pAAO precise valence and conductive band levels are unknown, though the bandgap is definitely larger when compared to the bulk counterpart due to quantum size effects

3.1.4 Light Emitting Diodes

Based on postulates of the Shockley-Queisser formulation [91] efficient solar cell absorber materials should also be good at emitting light. Recent success of perovskites as solar cell absorber material and developments in the field of quantum dot emitter materials, ncHP appear to be a very good candidate for next generation materials for optoelectronics applications which inlcude color-conversion, color-enhancer and quantum dot based LED screens [48]. Using ncHP confined within pAAO allows for a unique approach of using quantum dots prepared in device-ready architecture that is easily electrically addressable. In Fig.3.17A the structure of the LED prepared during this work is shown. At the heart of the device lies ncHP stacked inside a vertically propagating insulating pAAO matrix. The active material is sandwiched between hole transporting material (F8) and electron transporting material (TiO_2) in order to better match the energy levels of the materials (Fig.3.17B). The transparent electrode in this device is FTO on glass, while on the other side a Ag/MoO_3 electrode is used.

The LEDs were produced with two types of active material: $CsPbBr_3$ and $MAPbI_3$. The characteristic blue shift that was observed in the PL spectra could be also observed in the electroluminescence (EL) spectra, although a little bit shifted in both of the systems (Fig.3.18A, B). Fig.3.18A shows EL (dotted line) of a $CsPbBr_3$ LED compared to the materials bulk and confined PL. $CsPbBr_3$ EL is at 2.40 eV and shows narrow FWHM of only 0.09 eV that is blue
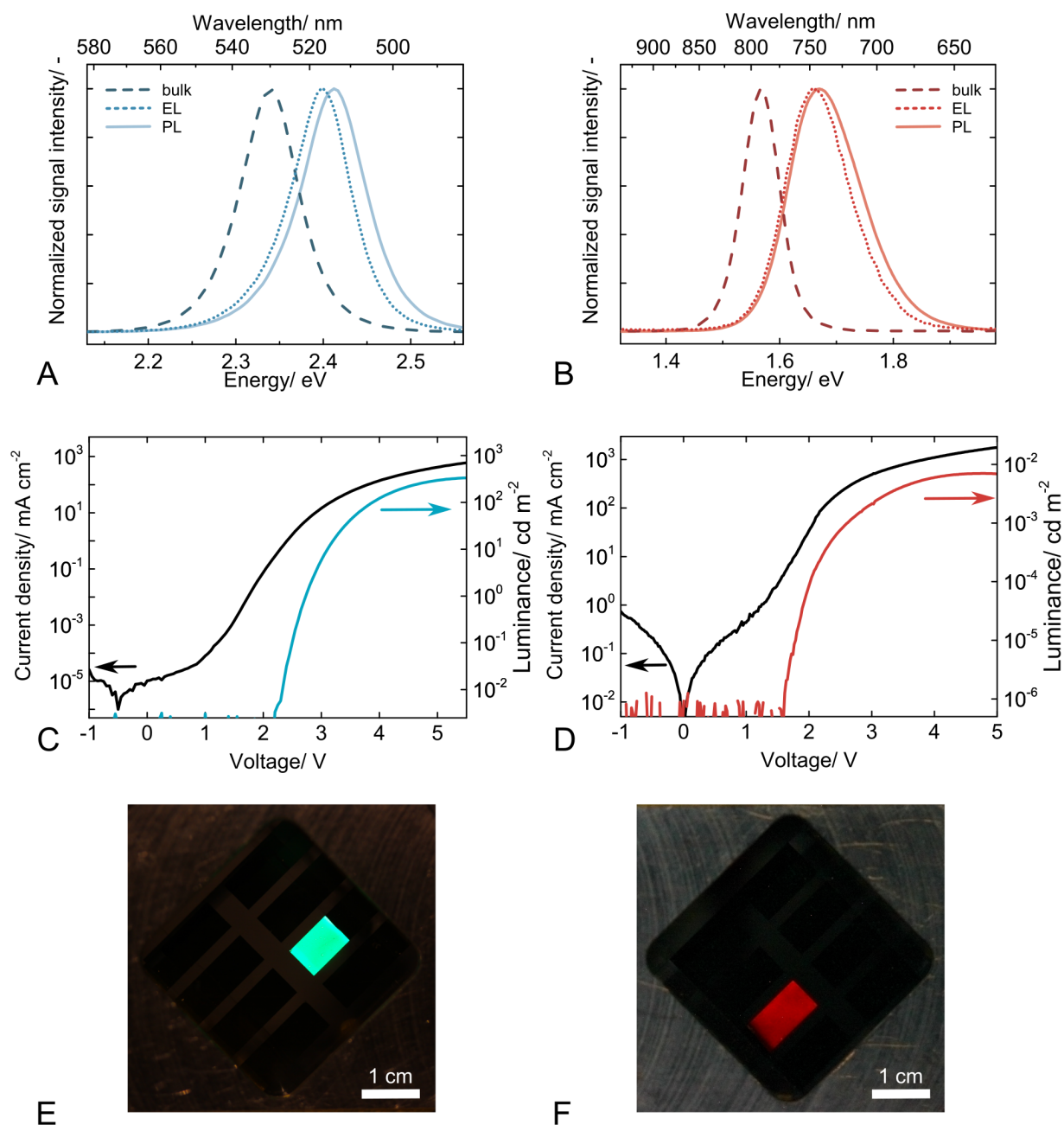
Figure 3.18: Comparison of bulk PL (dashed line), pAAO confined PL (solid line) and pAAO confined EL of A - $CsPbBr_3$ and B - $MAPbI_3$; current density and luminance of C - $CsPbBr_3$ and D - $MAPbI_3$ LEDs; visible emission could be observed with the naked eye in both E - $CsPbBr_3$ and $MAPbI_3$ containing device.

shifted by 0.06 eV from the bulk PL and 0.01 eV red-shifted from confined PL. Fig.3.18B shows EL (dotted line) of the $MAPbI_3$ system. $MAPbI_3$ EL has its maximum at 1.66 eV with FWHM of 0.14 eV that is 0.10 eV blueshifted when compared to the bulk PL and 0.01 eV shifted when compared to confined pAAO PL signal. $CsPbBr_3$ LEDs turn on at around 2.2 V and show 300 cd m^{-2} brightness at 5 V (Fig.3.18C). At its peak brightness around 420 mA cm^{-2} pass through a pixel, with a current efficiency of 0.09 cd A^{-1} and external quantum efficiency of ~0.03%. At 5 V the brightness of $MAPbI_3$ is 0.007 cd m^{-2} and 1.8 A cm^{-2} are passing through the device. Small luminance value in $MAPbI_3$ devices is partially due to low responsivity of the eye in the deep-red part of the spectra. Nevertheless, the high PLQY of this material as well as information available in the literature [92] suggests that further optimization is possible an higher brightness and efficiency can be achieved. Both of the devices showed EL observable with the naked eye that is homogeneous over the large area of a single pixel (15 mm^{-2}) (Fig.3.18E,F).

3.2 Low temperature spectroscopy

Temperature dependent PL spectroscopy is an excellent technique that can be used to acquire information about intrinsic properties of semiconductors and their charge carriers. The PL peak shape of semiconductor QDs is mainly influenced by exciton recombination, but also by QDs size distribution, energy trap states, exciton-phonon interactions, *etc.* At low temperatures the carriers are effectively frozen in their states while at room temperature they are being influenced by many different factors [93]. A comparison of low and room temperature emission allows to separate the various influences on the sample emission and to learn more about the fundamental nature of the materials.

The measurements were performed between 4 and 300 K for $MAPbBr_3$, $CsPbBr_3$ and $MAPbI_3$ on pAAO confined samples and bulk polycrystalline films on sapphire. The data was analyzed for changes in peak energy (energy corresponding to signal maximum), presence of additional peaks, changes in intensity (signal maximum), and peak broadening (difference in energy at peak half maximum). Using this information and the models mentioned below it was possible to calculate exciton binding energy (E_B), longitudinal optical phonon energy (E_{ph}), inhomogeneous broadening (Γ_0), and the exciton-phonon coupling strength (Γ_{op}) contribution to the broadening of the emission.

Besides band-gap exciton recombination there are other radiative recombination pathways which would contribute to the emission. Both $MAPbBr_3$ and $CsPbBr_3$ showed slight peak
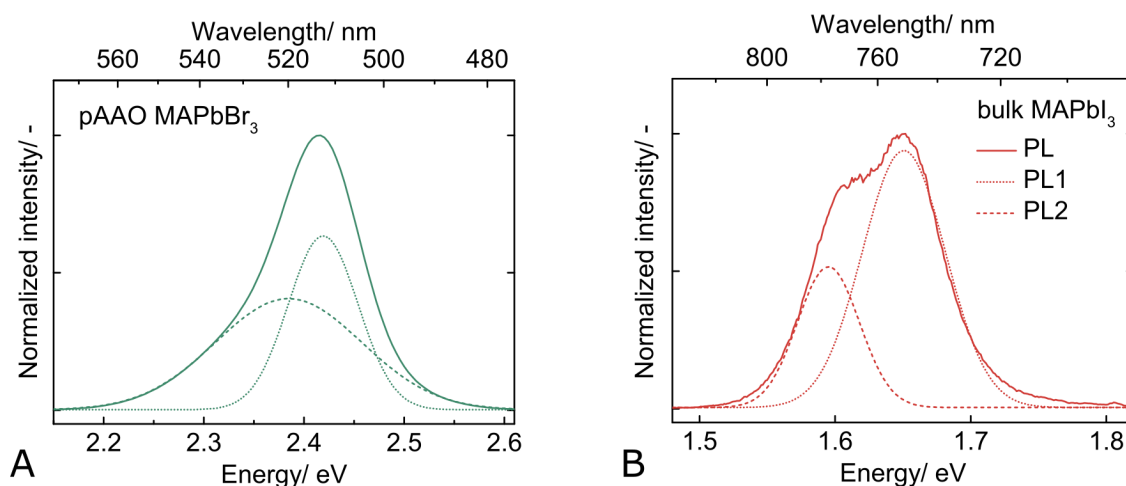
Figure 3.19: An example of peak broadening and peak splitting during the experiment. A - peak broadening on the lower energy side of the main emission for pAAO MAPbBr$_3$ sample at 4 K which disappears shortly as the temperature increases. An identical "shoulder" could also be observed in pAAO CsPbBr$_3$ samples; B - peak splitting observed at 180 K in bulk MAPbI$_3$ that signifies a phase transition that usually occurs in this material in the mid-temperature range. Separate peaks were labeled PL1 (higher energy) and PL2 (lower energy).

broadening on the lower energy side in the low temperature region that disappeared as the temperature increases (Fig.3.19A). Nevertheless the signal was not disturbed significantly and the whole range of data was used for analysis and model fitting. pAAO MAPbI$_3$ showed a relatively symmetric emission, while bulk MAPbI$_3$ displayed peak splitting in the mid-temperature region (Fig.3.19B). The peaks are addressed separately in the analysis and are labeled PL1 (higher in energy) and PL2 (lower in energy) (Fig.3.19B). Full model fitting was not possible for the bulk MAPbI$_3$ system.

Thermal quenching of the excitonic luminescence is studied via analysis of normalized intensity. Eq.3.5 has been used in literature to describe PL quenching processes in quantum dots [94], [95]:

$$I(T) = \frac{I_0}{1 + Ae^{-E/k_bT}} \tag{3.5}$$

where $I(T)$ - normalized integrated PL intensity at a certain temperature, I_0 - PL intensity at 0 K, A - a fitting parameter related to the strength of the quenching process, E - activation energy for thermal quenching of the excitonic luminescence, k_B - Boltzmann constant, and T - temperature. The two-step quenching model (eq.3.6) is based on a modified form of this equation, which assumes two non-radiative recombination channels related to the quenching mechanism of PL intensity (E_1 and E_2), where E_1 is often interpreted as the exciton binding

energy [96], [97]:

$$I(T) = \frac{I_0}{1 + A_1 e^{-E_1/k_b T} + A_2 e^{-E_2/k_b T}} \qquad (3.6)$$

Line broadening was analyzed by monitoring FWHM, as a function of increasing temperature. Signal broadening consists of two contributing factors: inhomogeneous (temperature independent) and homogeneous (temperature dependent) broadening. Inhomogeneous broadening is caused by size dispersion, shape, elemental composition of the material, or other related factors. Homogeneous broadening results due to exciton interaction with acoustic phonons, optical phonons, and possible impurities. In general, all of these interactions can be described using an independent boson model (eq.3.7):

$$\Gamma(T) = \underbrace{\Gamma_0}_{\text{inhomogeneous}} + \underbrace{\sigma T + \frac{\Gamma_{op}}{e^{E_{ph}/k_b T} - 1} + \Gamma_{imp} e^{-E_i/k_B T}}_{\text{homogeneous}} \qquad (3.7)$$

where $\Gamma(T)$ - FWHM of the signal, Γ_0 - inhomogeneous broadening, σ - exciton-acoustic phonon coupling, Γ_{op} - contribution of exciton-longitudinal optical (LO) phonon, Γ_{imp} - impurity contribution, E_{ph} - average phonon energy participating in the quenching process, k_b - Boltzmann constant, and T - temperature. One of the most prominent interactions in ionic or polar systems like perovskites are exciton-LO phonon Fröhlich interactions (Γ_{op}), which tend to govern signal broadening down to very low temperatures. The Γ_{imp} term is neglected during the following calculations due to the relatively low concentration of the trap states in perovskites.

3.2.1 MAPbBr$_3$

The results of the low temperature PL study of the MAPbBr$_3$ system are shown in Fig.3.20. In the case of both pAAO and bulk samples, a typical blue shift could be observed as the temperature increased from 4 to 300 K (Fig.3.20A). pAAO confined samples show emission at 2.35 eV for 4 K and 2.41 eV for 300 K. The bulk sample PL peak is located at 2.24 eV for 4 K and at 2.32 eV for 300 K. The observed shift is less pronounced in pAAO samples than in the bulk sample. This might suggest preservation of the tetragonal phase in higher amounts in Orthorhombic I and II phases at low temperatures. In classic semiconductors the signal tends to redshift with increasing temperatures, thus making perovskite peak shifting quite unusual [98]. The reason behind the blueshift in perovskites has been attributed to either multiphonon step-up processes, where the carriers obtain higher energy through phonon absorption which becomes more pronounced at higher temperatures [99] or thermal expansion of the crystal lattice and decreased electron-phonon interactions [75]. Nevertheless, the peak shifting behavior of both pAAO and bulk samples is in line with previous literature reports [79].
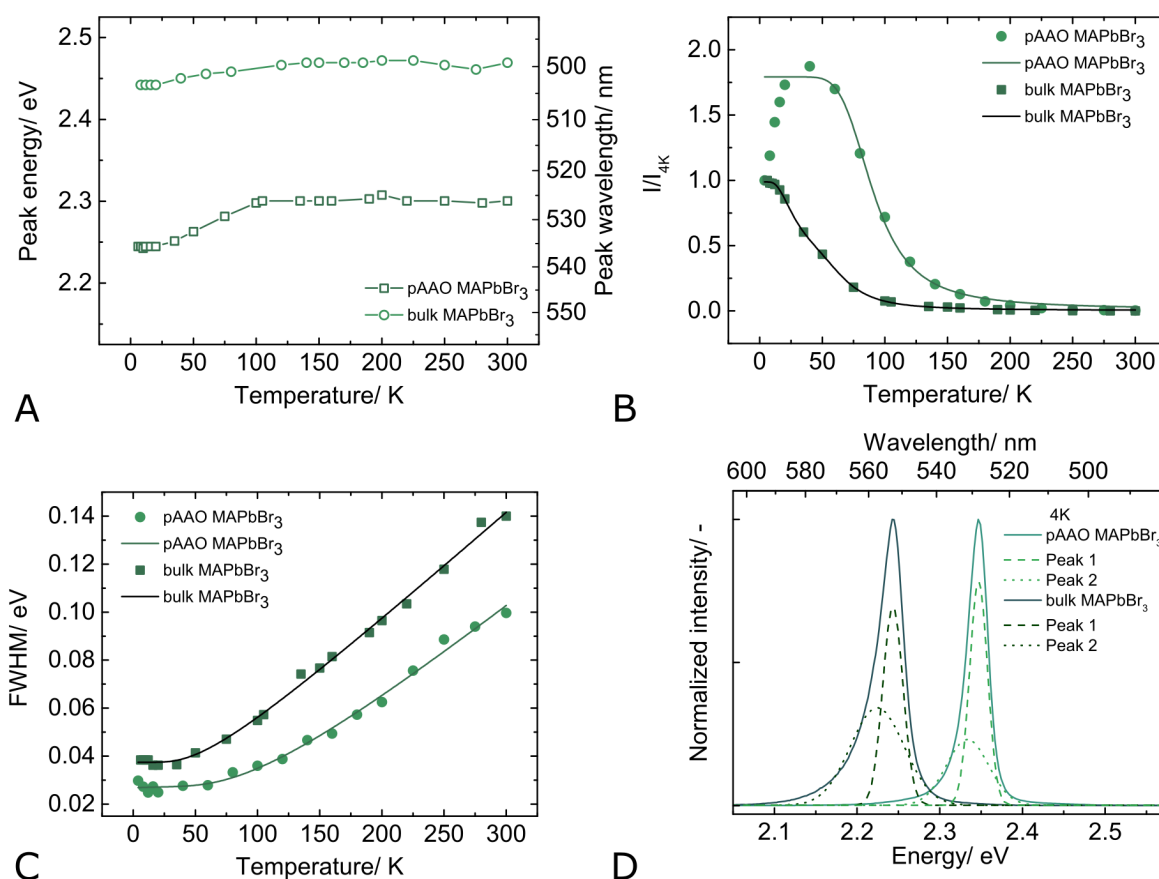
Figure 3.20: Low temperature spectroscopy results for MAPbBr$_3$ system. A - peak PL energy of pAAO (circles) and bulk (squares) PL as the function of increasing temperature; B - normalized intensity of pAAO (circles) and bulk (squares) samples as a function of increasing temperature showing an anomalous peak intensity in pAAO samples at around 50 K; C - FWHM through the range of temperatures for both in pAAO (circles) and bulk (squares) samples. The slight initial decrease of FWHM pAAO until *ca.*30 K might be contributed by the low temperature peak "shoulder" that disappears afterwards. D - pAAO (light green) and bulk (dark green) sample emissions at 4 K showing a "shoulder" on the lower energy side. The broadening feature is highlighted by fitting two Gaussian peaks to each of the signals.

The PL intensity tends to decrease as the temperature decreases. Interestingly, pAAO shows an anomalous intensity increase of almost 60% up to *ca.* 50 K, after which it continues to decrease all the way to 300 K (3.20B). The bulk sample PL intensity decreases with increasing temperature between 4 and 300 K. The data from pAAO (50 - 300 K) and bulk (4-300 K) was fitted using eq.3.6. When compared, $E_1 = 46\ meV$ in pAAO sample is larger than $E_1 = 35\ meV$ in bulk samples. The increase in E_1 is consistent with an increase of exciton binding energy due to the influence of quantum size effects. Other fitting parameters are shown in Tab.3.2. A similar PL intensity increase was previously observed in PbS QDs [93]. There it has been attributed to shallow trap states that capture carriers and release them into the ground state after a certain thermal activation energy has been reached, thus increasing the PL intensity.

Table 3.2: Intensity fitting parameters for pAAO and bulk MAPbBr$_3$ samples using eq.3.6.

	I_0/-	A_1/-	E_1/ meV	A_2/ -	E_2/ meV
pAAO	1.79	372	46	24	46
bulk	0.98	581	35	4	5

The peak broadening as a function of increasing temperature is summarized in Fig.3.20C. pAAO samples are consistently narrower throughout the whole range of temperatures when compared to bulk samples. The rate of FWHM decrease is the same for both pAAO and bulk samples. The initial slight decrease of FWHM in pAAO samples up until *ca.* 30 K can be attributed to peak broadening that can be observed at 4 K that then disappears at around 30 K. Similar broadening feature can be also observed in bulk samples though to a lesser degree (Fig.3.20D). This broadening can be attributed to an appearance of a second peak, which is highlighted by fitting two Gaussian peaks to the signal at 4 K in Fig.3.20D. The broadening has been reported in perovskite literature before, where the main band was attributed to exciton recombination and the broad band to phonon replicas [100] or bound exciton emission due to Br vacancy trap states [99]. Similar effects have been observed in PbS QDs where the broadening was described in terms of a phonon side band and separation between main band and the phonon band determined via Frank-Condon principles [93].

The FWHM data was fitted using eq.3.7 and it was observed that confined samples show increased exciton-LO phonon coupling, where $\Gamma_{op} = 84\ meV$ in confined samples and $\Gamma_{op} = 62\ meV$ in bulk samples. The increased Γ_{op} in confined samples can be explained by enhanced coupling of excitons with higher-frequency phonons [101]. Other fitting parameters are summarized in Tab.3.3.

Table 3.3: FWHM fitting parameters for pAAO and bulk MAPbBr$_3$ samples using eq.3.7.

	Γ_0/ meV	σ/ μeV K^{-1}	Γ_{op}/meV	E_{ph}/meV
pAAO	36	13	84	32
bulk	26	0.88	62	13

3.2.2 CsPbBr$_3$
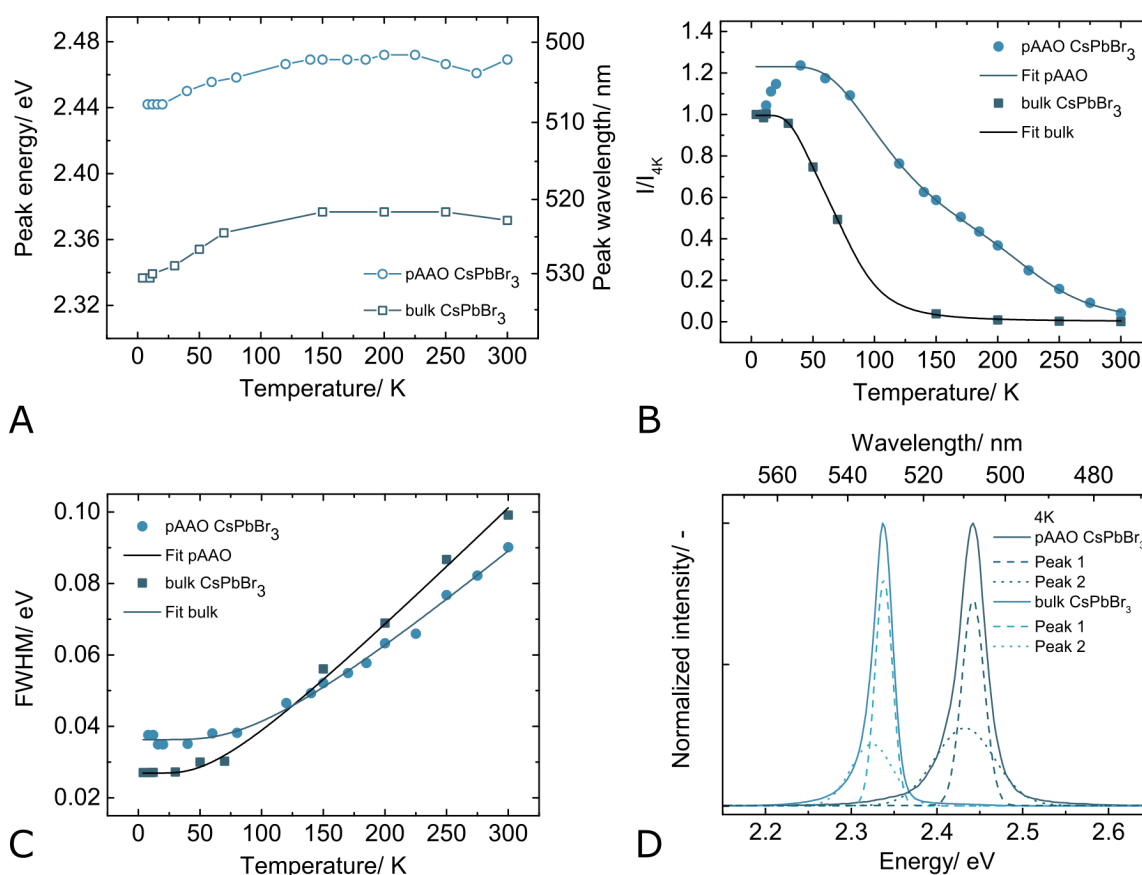
Figure 3.21: Low temperature spectroscopy results for the CsPbBr$_3$ system. A - peak PL energy of pAAO and bulk samples as a function of energy, showing a more pronounced blueshift in the low temperature part in pAAO when compared to the bulk samples; B - normalized PL intensity as a function of increasing temperature. An anomalous increase in PL intensity can be observed in pAAO samples at around 50 K; C - FWHM of pAAO (circles) and bulk (squares) samples between 4 and 300 K. Slightly decreasing FWHM values in pAAO samples at the beginning of the temperature range could be attributed to the low energy shoulder. D - comparison of pAAO (blue) and bulk (dark blue) PL at 4 K, highlighting the broadening features (dotted line) on the lower energy side of the main signals (dashed lines);

The results of low temperature spectroscopy on CsPbBr$_3$ pAAO and bulk samples are

summarized in Fig.3.21. As evident from Fig.3.21A, $CsPbBr_3$ also shows a typical perovskite blueshift that occurs with increasing temperature. At 4 K pAAO emits at 2.44 eV, while at 300 K it emits at 2.45 eV. In case of bulk samples, the PL signal is located at 2.34 eV at 4 K and 2.37 eV at 300 K. pAAO samples show smaller blueshift, when compared to bulk.

A summary of the thermal quenching behavior is shown in Fig.3.21B. In the same way as in $MAPbBr_3$, pAAO samples show an initial increase until 40 K by almost 25%, after which the intensity decreases steadily. Bulk samples show an initial region of stability until about 40 K after which the intensity also starts to decrease. The data was fitted (pAAO was fitted between 40 and 300 K, bulk - full range) with eq.3.6, which shows that $E_1 = 21\ meV$ in bulk samples and $E_2 = 14\ meV$ in pAAO. This corresponds to an increase of exciton binding energy in confined samples and matches the previously reported values for similarly sized quantum particles [99]. E_1 for a bulk sample is in good agreement with results measured before on a single crystal using low temperature spectroscopy [99] and Raman spectroscopy [102]. Further fitting parameters are summarized in Tab.3.4

Table 3.4: Intensity fitting parameters for pAAO and bulk $CsPbBr_3$ samples using eq.3.6.

	I_0/-	A_1/-	E_1/ meV	A_2/ -	E_2/ meV
pAAO	1.23	69571	21	11	30
bulk	0.99	8	14	1876	56

The thermal broadening behavior as analyzed for pAAO and bulk samples is outlined in Fig.3.21C. Both pAAO and bulk samples appear to show decreasing FWHM at first up to *ca.* 30 K, then proceed to increase as expected. The narrowing of the peak between 4 and 30 K can be explained by disappearing of the low energy "shoulder" at around the same temperature (Fig.3.21D). The data was fitted using eq.3.7, showing an increase in inhomogeneous broadening (pAAO $\Gamma_0 = 36\ meV$ and bulk $\Gamma_0 = 27\ meV$) and exciton-LO phonon interaction (pAAO $\Gamma_{op} = 85\ meV$ and bulk $\Gamma_{op} = 62\ meV$). The increase in inhomogeneous broadening has been observed in previous studies too [75]. Exciton-LO phonon interactions measured during this study appear to be larger when compared to previous literature reports [75]. Further fitting parameters are shown in Tab.3.5.

3.2.3 $MAPbI_3$

The $MAPbI_3$ system shows a more complex behavior during low temperature spectroscopy. pAAO samples, in general, behave similar to other confined samples in this study (Fig.3.22). A

Table 3.5: FWHM fitting parameters for pAAO and bulk CsPbBr$_3$ samples using eq.3.7.

	Γ_0/ meV	σ/ µeV K^{-1}	Γ_{op}/meV	E_{ph}/meV
pAAO	36	2	85	25
bulk	27	0	62	16

typical blue shift is pronounced only between 4 and 150 K, where the peak shifts from 1.63 eV to 1.68 eV. After that the peak position remains relatively stable all the way to 300 K (Fig.3.22A). PL intensity, as in the other confined samples, increases dramatically almost by 60% in the low temperature range, after which it proceeds to decrease in a predictable manner (Fig.3.22B). The data points for the mid and high temperature range, where the intensity decreases with increasing temperature, is fitted with eq.3.6 showing an E_1 value of $58\ meV$. The broadening of the PL signal increased with the increasing temperature (Fig.3.22C). The model from eq.3.7 fitted the data pretty well with some minor deviation. Interestingly, pAAO samples also show a slight decrease in FWHM in the low temperature regime, even though no significant "shoulder" could be observed in the spectra at low temperatures (Fig.3.22D). Fitting parameters for both intensity and broadening profile are summarized in Tab.3.7.

Bulk MAPbI$_3$ exhibits a more complex PL temperature response (Fig.3.23). Due to a crystal phase transition from orthorhombic to tetragonal at around 150 K it is possible to observe strong PL shift as well as PL splitting (Fig.3.23A). The latter complicates analysis and interpretation of the PL signals as a function of temperature with the previously used models. The signal was fitted with two Gaussian peaks in order to account for the high energy peak (PL1) and low energy peak (PL2) that is is present in the range between 4 and 300 K (as previously described in 3.19B). The PL2 peak is present in the region between 4 and 75 K in a form of broadening and then splits into a unique peak at around 100 K, after which it redshifts until disappearing at around 200 K. The PL1 peak blueshifts between 4 and 150 K, where it reaches a tipping point and starts to redshift until 200 K. After 200 K the peak PL emission remains relatively constant. These transitions and peak shifting are in line with previous literature reports [103].

The intensity profile of bulk MAPbI$_3$ was also analyzed separately for PL1 and PL2 peaks (Fig.3.23C). It appears that the PL1 peak also shows an unusual increase in PL intensity at around 50 K which is not observed in the PL2 peak intensity pattern. On the other hand, the PL2 peak shows a slight increase in intensity right before disappearing at 200 K, which might be an artifact of two peaks merging. Both data sets were fitted with eq.3.6 and the fitting
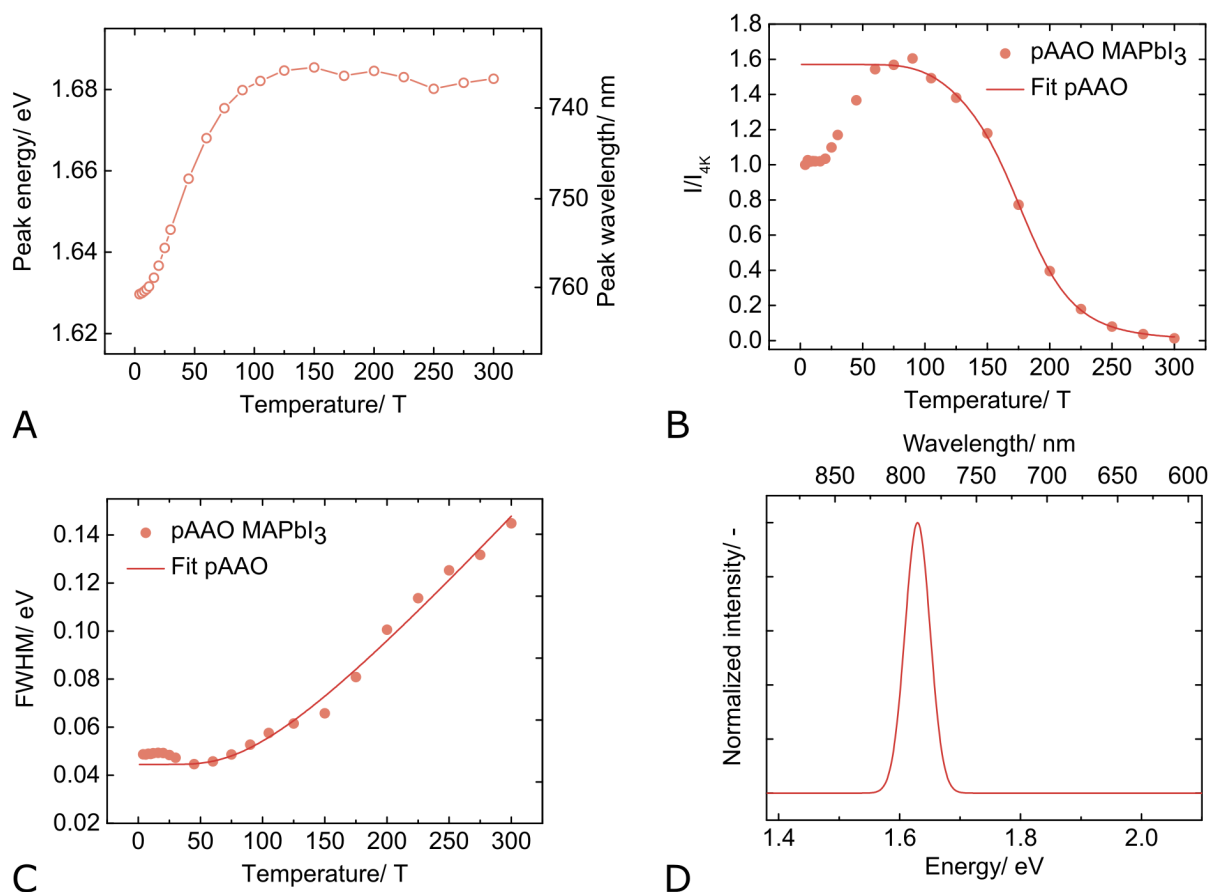
Figure 3.22: pAAO MAPbI$_3$ PL trends during low temperature spectroscopy. A - PL signal blueshifts as the temperature increases up to *ca.*150 K, after which the peak position remains relatively constant; B -PL peak intensity initially increases by up to 60% till the sample reaches *ca.* 100 K, after which the signal is thermally quenched; C - PL signal broadening with the increasing temperature; D - PL peak shape at 4 K is symmetric and displays no additional features;
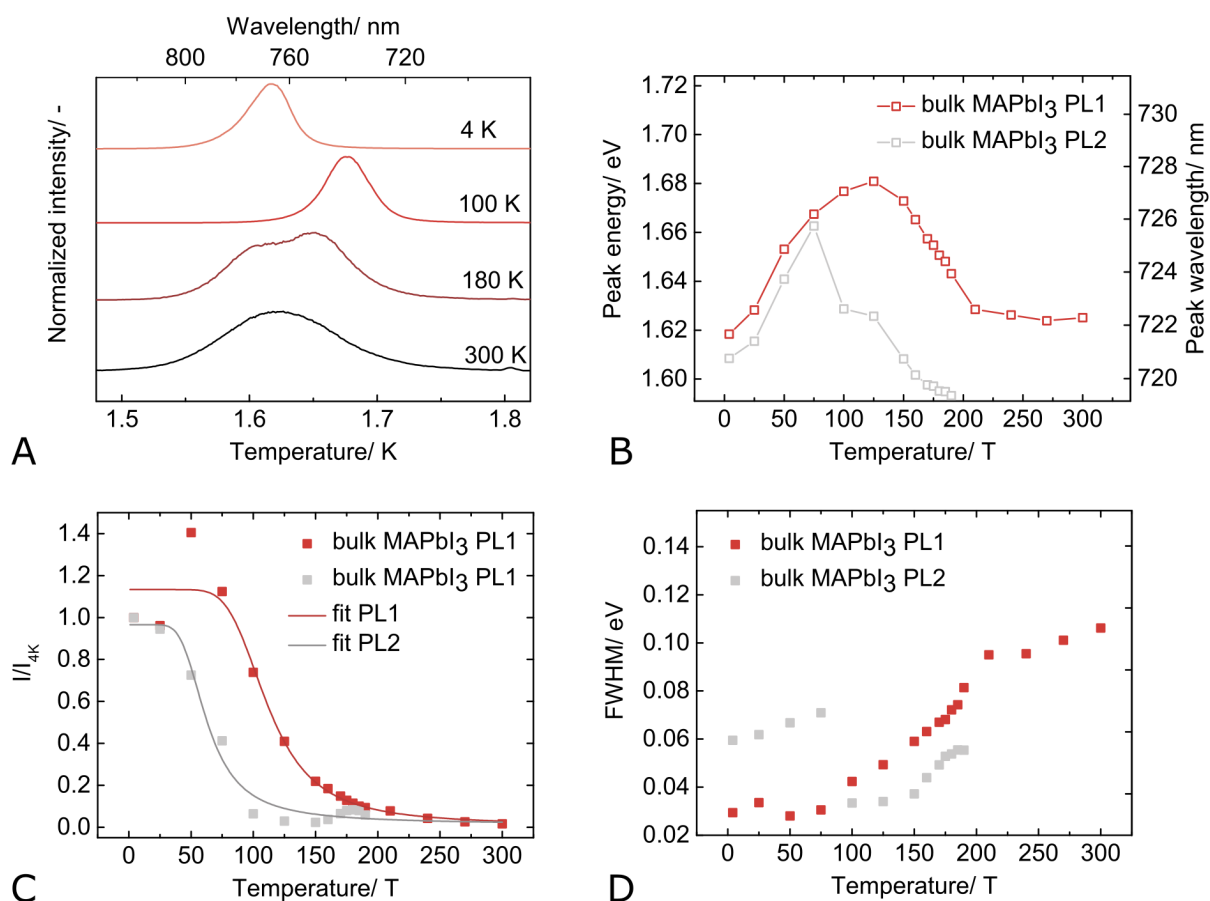
Figure 3.23: MAPbI₃ PL peak splitting and position shifting investigation during low temperature spectroscopy; A - pAAO PL at 4 K (red) and 300 K (gray) showing a broadening on the high energy side of the signal with no peak splitting observed in between; B - tracking of the peak emission energy throughout the temperature range. Blue shift that is typical for perovskites is observed with increasing temperatures in both PL1 (full circles) and PL2 (empty circles) peaks; C - bulk peak shape showing considerably more complex behavior when compared to pAAO sample. Examples of PL signal at 4 K, 100 K, 180 K, and 300 K shows broadening, splitting and single peak all present in bulk samples at different temperatures; D - bulk sample peak emission energy recorded at different temperatures. The sample shows a low energy broadening between 4 and 80 K, peak splitting between 80 and 190 K and only a single peak between 190 and 300 K.

Table 3.6: Intensity fitting parameters for pAAO and bulk MAPbI$_3$ samples using eq.3.6.

	I_0/-	A_1/-	E_1/ meV	A_2/ -	E_2/ meV
pAAO	1.57	251	58	80096	182
bulk PL1	1.13	210	57	133	58
bulk PL2	0.97	43	73	107	26

Table 3.7: FWHM fitting parameters for pAAO MAPbI$_3$ samples using eq.3.7.

	Γ_0/ meV	σ/ µeV k^{-1}	Γ_{op}/meV	E_{ph}/meV
pAAO	45	0	170	25

parameters are summarized in Tab.3.6.

The broadening profile of the PL1 peak is drastically different from the PL2 peak. The PL1 peak follows generally increasing FWHM with increasing temperature with a number of irregularities. The PL2 peak initially broadens until 100 K where it abruptly becomes significantly thinner and continues to broaden until 200 K. Neither of the peaks were evaluated with eq.3.7 due their complex behavior.

When comparing pAAO and bulk samples it evident that the confinement has a strong effect on the material properties. pAAO samples have flatter peak energy profile, which shows no peak splitting or any other strong transitions. Another effect is the appearance of intensity peak at around 50 K. These two phenomena indicate that there might be influence of geometrical constrains and quantum size effects on crystal phase transition, which would be important to investigate further in these and other perovskite systems.

3.3   Lead free 2D perovskites

Although Pb-containing HP have achieved a large degree of success, future mass application in optoelectronic devices will be hindered by the significant health hazard and possible environmental danger posed by these materials. Several different alternatives have been investigated in the literature, including MASnI$_3$ [104] and MAGeI$_3$ [105], though both of the materials are very easily oxidized (Sn^{2+} $\longrightarrow$ Sn^{4+} and Ge^{2+} $\longrightarrow$ Ge^{4+}). Recently several transition metal perovskites came to light as possible stable, earth-abundant, and cost-effective alternatives to Pb-containing HP [106], [62], [63]. Due to their relaxed geometrical constrains, this group of materials can incorporate a wider range of component ions and permits a higher degree of
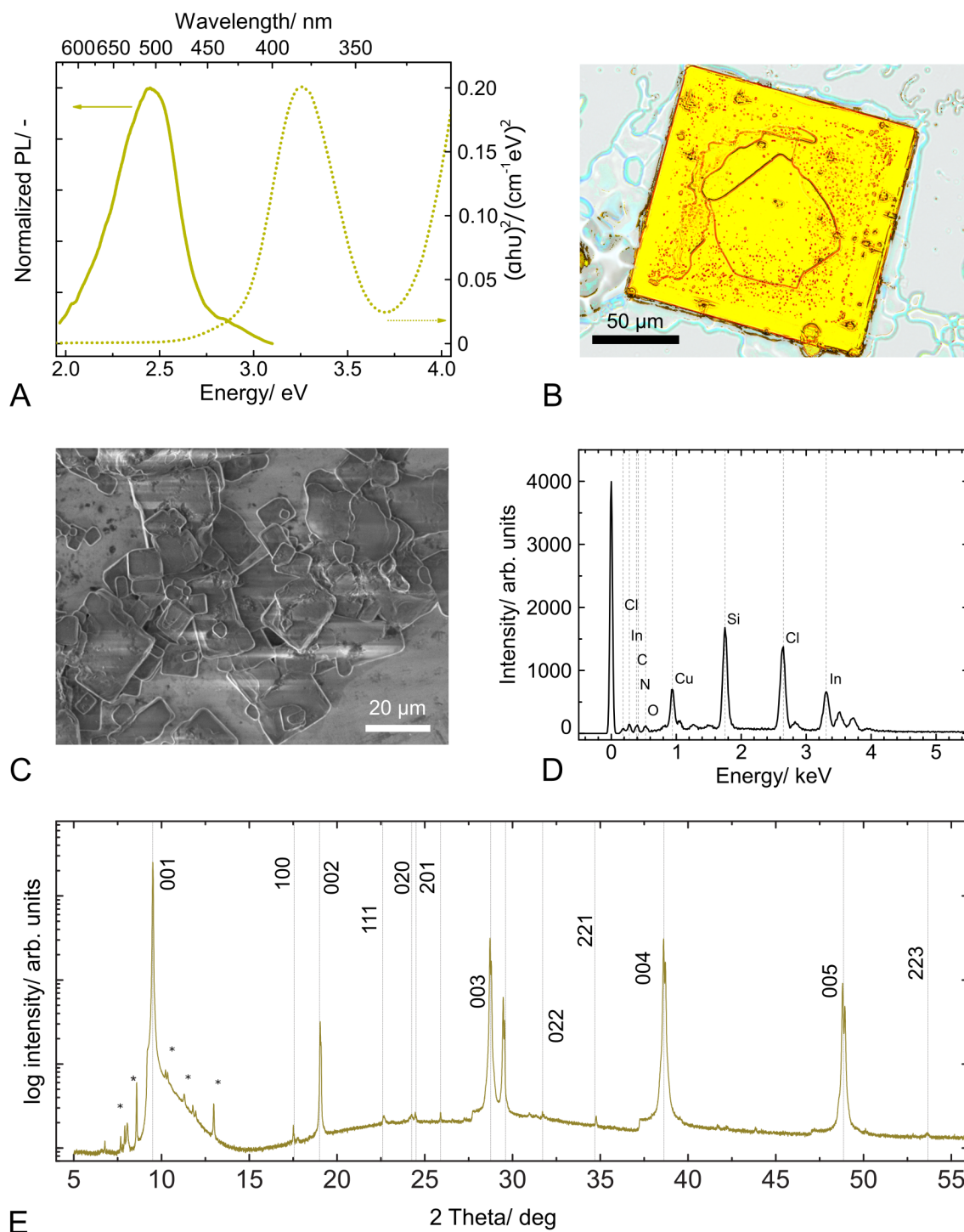
Figure 3.24: $(MA)_2CuCl_4$ optical and structural characterization. A - PL and thin film absorption; B - SEM of an island of $(MA)_2CuCl_4$ on ITO showing characteristic thin square crystals; C - thin film XRD on glass showing characteristic peaks describing 1D Ruddlesden-Popper structure; D - EDX analysis of $(MA)_2CuCl_4$ on ITO showing corresponding chemical elements present in the sample; E - XRD diffractogram showing peaks characteristic of $(MA)_2CuCl_4$; peaks marked with a star do not belong to $(MA)_2CuCl_4$ and can result from residual $MAPbCl_2$ or $CuCl_2$ still present in the thin film.

tunability.

During this work Cu-based lead-free 2D HP $(MA)_2CuCl_4$ was investigated due to Cu^{2+} stability in aerobic environments. The material was synthesized using a modified procedure reported by Coreteccia *et al.* [63]. Drop-casted thin films showed characteristic PL with a peak at 2.45 eV and FWHM of 0.39 eV as well as an absorption profile previously described in the literature [63] (Fig.3.24A). Single crystal platelets of $(MA)_2CuCl_4$ with an edge size up to 150 μm were grown from saturated EtOH solution by gradual evaporation of solvent, following the procedure reported in literature [107]. As expected, single crystals were square shaped and had yellow color (Fig.3.24B). SEM image of $(MA)_2CuCl_4$ drop-casted on ITO substrate using DMSO precursor solution also shows characteristic square platelets although in this particular case with more defects and twinned crystals (Fig.3.24C). An EDX analysis was performed on the sample in order to confirm the nature of the formed crystals. Characteristic peaks for Cl, C, N, and Cu were observed, which can be assigned to the elements found in $(MA)_2CuCl_4$. Presence of In, Si and O can be explained by the substrate composition. An XRD analysis was performed to confirm the identity of the formed thin film and its crystaline structure. Based on the previously reported diffractograms [63], it was possible to assign almost all of the peaks to a specific crystallographic orientation and the Ruddlesden-Popper 2D structure of $(MA)_2CuCl_4$ was confirmed. Extremely strong $(00l)$ peaks suggest a high degree of crystallinity and preferential orientation parallel to the surface of the substrate [the (001) plane]. Four small peaks between 8 and 14° are not usually present in $(MA)_2CuCl_4$ and can be explained by presence of residual MAPbCl or $CuCl_2$. Based on the XRD pattern, unit cell distances could be calculated (a = 7.27 Å, b = 7.32 Å, c = 9.95 Å) and when compared with the previously reported values are good agreement with them [63]. $(MA)_2CuCl_4$ exhibits issues relating to charge carrier transport that limits its performance in optoelectronic devices [63]. Controlled crystallization in order to preferentially orient the structure perpendicular to substrate surface might offer a solution. pAAO was investigated as a possible matrix which would allow a certain degree of control of the orientation of the crystal, though unfortunately no PL emission was observed from these films.

4 Conclusion

During this work a new method to prepare ncHP has been demonstrated. ncHP were grown inside porous oxide thin films with nanometer-scale pore diameter thus limiting and controlling their crystalline size. Four different HP systems were investigated during this work, which included organic-inorganic hybrid halide perovskites like $MAPbCl_3$, $MAPbBr_3$, and $MAPbI_3$, as well as fully inorganic $CsPbBr_3$. Strong size dependent effects attributed to quantum confinement were observed in all of the systems. The PL of ncHP was significantly blue shifted when compared to bulk emission. Additional control over the position of the confined peak was achieved via changing the size of the pore diameter in the oxide matrix. Stronger hypsochromic shifts were observed in the pSi system, due to smaller size of the pores (< 2 nm). Nevertheless, pAAO samples also showed significant blue shift although with lesser degree of tunability. Confinement effects were shown in both single halide and mixed halide systems, presenting the universality of the ncHP preparation approach. Color purity of ncHP PL emission in both pSi and pAAO was compared to existing RGB color spaces, showing exceptional performance that can potentially compete with existing LED technology, industry issued standards, and recommendations.

Further optical characterization of the sample included PL lifetime measurements in pSi samples with smallest (prepared in pSi etched at 5 mA cm^{-2}) and largest pores (prepared in pSi etched at 30 mA cm^{-2}), showing general trend of decreasing radiative lifetime in smaller quantum dots. PL stability of ncHP ($MAPbBr_3$ and $CsPbBr_3$) in pAAO under ambient conditions and constant illumination was compared with their bulk counterparts. pAAO samples showed not only increased PL stability, but also an initial PL intensity increase of over 30%. No unified conclusion as to the nature of the observed behavior has been reached in the previously reported literature, therefore suggesting new avenues for future investigations.

Additionally, SEM and TEM structural characterization was performed on the ncHP in porous oxide matrices. It was confirmed that the morphology of pSi and pAAO differ significantly, where pSi exhibits a disordered sponge like inter-penetrating network of pores, while

pAAO consists of randomly distributed pores all perpendicularly oriented to the surface of the substrate. The nature of the embedded nanoparticles, as well as a first approximation of their size (~4 nm) was done using EDX analysis.

High energy X-ray diffraction studies (WAXS and SAXS) were performed in order to investigate the structure of the npHP as well as the surrounding oxide matrix. The crystallite size of ncHP embedded in pSi etched at 15, 25, and 30 mA cm^{-2} were determined to be 1.8, 2.1, and 4.5 nm respectively. The porosity of 15 mA cm^{-2} pSi matrix was studied with a Porod method and determined to be 57% with an average pore diameter of 40 Å.

A proof-of-concept LED was prepared using $CsPbBr_3$ and $MAPbI_3$ ncHP embedded in pAAO material as the active emitting material. The $CsPbBr_3$ system was used to prepare green emitting LEDs that achieved a luminance of ~300 cd m^{-2}, which reaches indoor-display brightness levels. The $MAPbI_3$ system was used to prepare red LEDs which showed significantly lower luminance, but still were visible to the naked eye. Electrical performance of the LEDs shows room for improvement, namely by selecting a more appropriate HTL and layer making further adjustments to the device architecture.

Low temperature spectroscopy measurements were performed on pAAO samples of $MAPbBr_3$, $CsPbBr_3$ and $MAPbI_3$ in the range between 4 and 300 K. The results were also compared to their corresponding bulk films. In all cases, bulk samples displayed regular behavior that is in line with previous literature reports. On the other hand, pAAO samples showed an anomalous intensity profile, with significant increase in the region below 100 K. This phenomenon has not been reported in literature and would require further investigation to fully understand its nature.

The Pb-free transition metal perovskite $(MA)_2CuCl_4$ was investigated as potential next generation non-toxic light emitting material. Thin films of $(MA)_2CuCl_4$ were synthesized on glass substrate and a number of optical and structural analyses were performed to confirm the nature of the synthesized material. No PL emission was observed upon deposition of $(MA)_2CuCl_4$ on pAAO. Further improvements can be achieved by selecting an appropriate solvent mixture and adjusting the size of the pores.

List of Figures

List of Tables

Bibliography

[1] Peter Atkins and Julio De Paula. *Elements of physical chemistry*. Oxford University Press, USA, 2013.

[2] Paras N Prasad. *Nanophotonics*. John Wiley & Sons, 2004.

[3] Leonid Gurevich, Luca Canali, Leo P Kouwenhoven, Erik PAM Bakkers, and Daniel Vanmaekelbergh. Electron confinement and single electron effects in metallic and semiconducting nano-clusters. *Phys. Rev. B*, 62:2614–1618, 2000.

[4] William Frank, Warren Hauptin, Helmut Vogt, Bruno Marshal, Jomar Thonstad, Robert Dawless, Halvor Kvande, and Oyebode Taiwo. Ullmann's encyclopedia of industrial chemistry, 2012.

[5] Silicon. Web: <http://periodic.lanl.gov/14.shtml>, February 2018.

[6] Michael J Sailor. *Porous silicon in practice: preparation, characterization and applications*. John Wiley & Sons, 2012.

[7] A Uhlir. Electrolytic shaping of germanium and silicon. *Bell Labs Technical Journal*, 35(2):333–347, 1956.

[8] V Lehmann and Ulrich Gösele. Porous silicon formation: A quantum wire effect. *Applied Physics Letters*, 58(8):856–858, 1991.

[9] AV Alexeev-Popov, SA Gevelyuk, Ya O Roizin, DP Savin, and SA Kuchinsky. Diffraction gratings on porous silicon. *Solid state communications*, 97(7):591–593, 1996.

[10] Bernard Gelloz and Nobuyoshi Koshida. Electroluminescence with high and stable quantum efficiency and low threshold voltage from anodically oxidized thin porous silicon diode. *Journal of Applied Physics*, 88(7):4319–4324, 2000.

[11] Leigh T Canham. Bioactive silicon structure fabrication through nanoetching techniques. *Advanced Materials*, 7(12):1033–1037, 1995.

[12] AG Khokhlov, RR Valiullin, MA Stepovich, and J Kärger. Characterization of pore size distribution in porous silicon by nmr cryoporosimetry and adsorption methods. *Colloid Journal*, 70(4):507–514, 2008.

[13] R Herino, G Bomchil, K Barla, C Bertrand, and J Lj Ginoux. Porosity and pore size distributions of porous silicon layers. *Journal of the electrochemical society*, 134(8):1994–2000, 1987.

[14] Claude Lévy-Clément, Abdelghani Lagoubi, and Micha Tomkiewicz. Morphology of porous n-type silicon obtained by photoelectrochemical etching i. correlations with material and etching parameters. *Journal of The Electrochemical Society*, 141(4):958–967, 1994.

[15] V Lehmann and S Ronnebeck. The physics of macropore formation in low-doped p-type silicon. *Journal of The Electrochemical Society*, 146(8):2968–2975, 1999.

[16] Hiroshi Sugiyama and Osamu Nittono. Microstructure and lattice distortion of anodized porous silicon layers. *Journal of Crystal Growth*, 103(1-4):156–163, 1990.

[17] RB Wehrspohn, J-N Chazalviel, and F Ozanam. Macropore formation in highly resistive p-type crystalline silicon. *Journal of The Electrochemical Society*, 145(8):2958–2961, 1998.

[18] Leigh Canham. *Handbook of porous silicon*. Springer, 2014.

[19] MN Obrovac and Leif Christensen. Structural changes in silicon anodes during lithium insertion/extraction. *Electrochemical and Solid-State Letters*, 7(5):A93–A96, 2004.

[20] Emily J Anglin, Lingyun Cheng, William R Freeman, and Michael J Sailor. Porous silicon in drug delivery devices and materials. *Advanced drug delivery reviews*, 60(11):1266–1277, 2008.

[21] S Chan, PM Fauchet, Y Li, LJ Rothberg, and BL Miller. Porous silicon microcavities for biosensing applications. *physica status solidi (a)*, 182(1):541–546, 2000.

[22] Jimmy WP Bakker, Hans Arwin, Guoliang Wang, and K Järrendahl. Improvement of porous silicon based gas sensors by polymer modification. *Physica status solidi (a)*, 197(2):378–381, 2003.

[23] Cornel Cobianu, Cristian Savaniu, Octavian Buiu, Dan Dascalu, Maria Zaharescu, Constanta Parlog, Albert Van Den Berg, and Bela Pecz. Tin dioxide sol–gel derived thin films deposited on porous silicon. *Sensors and Actuators B: Chemical*, 43(1-3):114–120, 1997.

[24] AJ Fernandes, PJ Ventura, RF Silva, and MC Carmo. Porous silicon capping by cvd diamond. *Vacuum*, 52(1-2):215–218, 1999.

[25] Keiki-Pua S Dancil, Douglas P Greiner, and Michael J Sailor. A porous silicon optical biosensor: detection of reversible binding of igg to a protein a-modified surface. *Journal of the American Chemical Society*, 121(34):7925–7930, 1999.

[26] D Clement, J Diener, E Gross, N Künzner, V Yu Timoshenko, and D Kovalev. Highly explosive nanosilicon-based composite materials. *physica status solidi (a)*, 202(8):1357–1364, 2005.

[27] J Mizsei. Gas sensor applications of porous si layers. *Thin solid films*, 515(23):8310–8315, 2007.

[28] Hariharsudan Sivaramakrishnan Radhakrishnan, Chihak Ahn, Jan Van Hoeymissen, Frédéric Dross, Nick Cowern, Kris Van Nieuwenhuysen, Ivan Gordon, Robert Mertens, and Jef Poortmans. Gettering of transition metals by porous silicon in epitaxial silicon solar cells. *physica status solidi (a)*, 209(10):1866–1871, 2012.

[29] William Frank, Warren Hauptin, Helmut Vogt, Bruno Marshal, Jomar Thonstad, Robert Dawless, Halvor Kvande, and Oyebode Taiwo. Ullmann's encyclopedia of industrial chemistry, 2012.

[30] Keith Hudson, Chanakya Misra, Anthony Perrotta, Karl Wefers, and F. Williams. Ullmann's encyclopedia of industrial chemistry, 2012.

[31] Heinrich Buff. Ueber das electrische verhalten des aluminiums. *European Journal of Organic Chemistry*, 102(3):265–284, 1857.

[32] Woo Lee and Sang-Joon Park. Porous anodic aluminum oxide: anodization and templated synthesis of functional nanostructures. *Chemical reviews*, 114(15):7487–7556, 2014.

[33] Hideki Masuda, Haruki Yamada, Masahiro Satoh, Hidetaka Asoh, Masashi Nakao, and Toshiaki Tamamura. Highly ordered nanochannel-array architecture in anodic alumina. *Applied Physics Letters*, 71(19):2770–2772, 1997.

[34] Hideki Masuda and Kenji Fukuda. Ordered metal nanohole arrays made by a two-step replication of honeycomb structures of anodic alumina. *science*, 268(5216):1466–1468, 1995.

[35] JP O'sullivan and GC Wood. The morphology and mechanism of formation of porous anodic films on aluminium. *Proc. R. Soc. Lond. A*, 317(1531):511–543, 1970.

[36] François Le Coz, Laurent Arurault, and Lucien Datas. Chemical analysis of a single basic cell of porous anodic aluminium oxide templates. *Materials characterization*, 61(3):283–288, 2010.

[37] Joshua T Smith, Qingling Hang, Aaron D Franklin, David B Janes, and Timothy D Sands. Highly ordered diamond and hybrid triangle-diamond patterns in porous anodic alumina thin films. *Applied Physics Letters*, 93(4):043108, 2008.

[38] Sarah E Brunker, Kristin B Cederquist, and Christine D Keating. Metallic barcodes for multiplexed bioassays. 2007.

[39] Haining Chen, Zhanhua Wei, Xiaoli Zheng, and Shihe Yang. A scalable electrodeposition route to the low-cost, versatile and controllable fabrication of perovskite solar cells. *Nano Energy*, 15:216–226, 2015.

[40] Peng Chen, Toshiyuki Mitsui, Damon B Farmer, Jene Golovchenko, Roy G Gordon, and Daniel Branton. Atomic layer deposition to fine-tune the surface properties and diameters of fabricated nanopores. *Nano letters*, 4(7):1333–1337, 2004.

[41] Masashi Nakao, Satoshi Oku, Hidenao Tanaka, Yasuo Shibata, Atsushi Yokoo, Toshiaki Tamamura, and Hideki Masuda. Fabrication of gaas hole array as a 2d-photonic crystal and their application to photonic bandgap waveguide. *Optical and quantum electronics*, 34(1-3):183–193, 2002.

[42] JX Ding, JA Zapien, WW Chen, Y Lifshitz, ST Lee, and XM Meng. Lasing in zns nanowires grown on anodic aluminum oxide templates. *Applied physics letters*, 85(12):2361–2363, 2004.

[43] Ioannis L Liakos, Roger C Newman, Eoghan McAlpine, and Morgan R Alexander. Comparative study of self-assembly of a range of monofunctional aliphatic molecules on magnetron-sputtered aluminium. *Surface and interface analysis*, 36(4):347–354, 2004.

[44] Merlin L Bruening, David M Dotzauer, Parul Jain, Lu Ouyang, and Gregory L Baker. Creation of functional membranes using polyelectrolyte multilayers and polymer brushes. *Langmuir*, 24(15):7663–7673, 2008.

[45] Phillip Szuromi and Brent Grocholski. Natural and engineered perovskites, 2017.

[46] Nobelprize.org. The nobel prize in physics 1987. Web: <http://www.nobelprize.org/nobel_prizes/physics/laureates/1987/>, February 2018.

[47] Mike Glazer. Bragg lecture 2017: The wondrous world of perovskites (discourse). Web: <https://www.youtube.com/watch?v=v9bMEUr2II4>, February 2018.

[48] Maksym V Kovalenko, Loredana Protesescu, and Maryna I Bodnarchuk. Properties and potential optoelectronic applications of lead halide perovskite nanocrystals. *Science*, 358(6364):745–750, 2017.

[49] Victor Moritz Goldschmidt. Die gesetze der krystallochemie. *Naturwissenschaften*, 14(21):477–485, 1926.

[50] Best research-cell efficiencies. Web: <https://www.nrel.gov/pv/assets/images/efficiency-chart.png>, February 2018.

[51] Horace Lemuel Wells. Über die cäsium-und kalium-bleihalogenide. *Zeitschrift für anorganische und allgemeine Chemie*, 3(1):195–210, 1893.

[52] CHR KN Møller. Crystal structure and photoconductivity of caesium plumbohalides. *Nature*, 182(4647):1436, 1958.

[53] Samuel D Stranks and Henry J Snaith. Metal-halide perovskites for photovoltaic and light-emitting devices. *Nature nanotechnology*, 10(5):391, 2015.

[54] Loredana Protesescu, Sergii Yakunin, Maryna I Bodnarchuk, Franziska Krieg, Riccarda Caputo, Christopher H Hendon, Ruo Xi Yang, Aron Walsh, and Maksym V Kovalenko. Nanocrystals of cesium lead halide perovskites (cspbx3, x= cl, br, and i): novel optoelectronic materials showing bright emission with wide color gamut. *Nano letters*, 15(6):3692–3696, 2015.

[55] Dmitry N Dirin, Loredana Protesescu, David Trummer, Ilia V Kochetygov, Sergii Yakunin, Frank Krumeich, Nicholas P Stadie, and Maksym V Kovalenko. Harnessing defect-tolerance at the nanoscale: Highly luminescent lead halide perovskite nanocrystals in mesoporous silica matrixes. *Nano letters*, 16(9):5866–5874, 2016.

[56] Stepan Demchyshyn, Janina Melanie Roemer, Heiko Groiß, Herwig Heilbrunner, Christoph Ulbricht, Dogukan Apaydin, Anton Böhm, Uta Rütt, Florian Bertram, Günter Hesser, et al. Confining metal-halide perovskites in nanoporous thin films. *Science advances*, 3(8):e1700738, 2017.

[57] Christopher Eames, Jarvist M Frost, Piers RF Barnes, Brian C O'regan, Aron Walsh, and M Saiful Islam. Ionic transport in hybrid lead iodide perovskite solar cells. *Nature communications*, 6:7497, 2015.

[58] Federica Bertolotti, Loredana Protesescu, Maksym V Kovalenko, Sergii Yakunin, Antonio Cervellino, Simon JL Billinge, Maxwell W Terban, Jan Skov Pedersen, Norberto Masciocchi, and Antonietta Guagliardi. Coherent nanotwins and dynamic disorder in cesium lead halide perovskite nanocrystals. *ACS nano*, 11(4):3819–3831, 2017.

[59] Zewen Xiao, Weiwei Meng, Jianbo Wang, David B Mitzi, and Yanfa Yan. Searching for promising new perovskite-based photovoltaic absorbers: the importance of electronic dimensionality. *Materials Horizons*, 4(2):206–216, 2017.

[60] Hsinhan Tsai, Wanyi Nie, Jean-Christophe Blancon, Constantinos C Stoumpos, Chan Myae Myae Soe, Jinkyoung Yoo, Jared Crochet, Sergei Tretiak, Jacky Even, Aditya Sadhanala, et al. Stable light-emitting diodes using phase-pure ruddlesden–popper layered perovskites. *Advanced Materials*, 2018.

[61] Hsinhan Tsai, Wanyi Nie, Jean-Christophe Blancon, Constantinos C Stoumpos, Reza Asadpour, Boris Harutyunyan, Amanda J Neukirch, Rafael Verduzco, Jared J Crochet, Sergei Tretiak, et al. High-efficiency two-dimensional ruddlesden–popper perovskite solar cells. *Nature*, 536(7616):312, 2016.

[62] Zhonghao Nie, Jie Yin, Huawei Zhou, Ning Chai, Baoli Chen, Yingtian Zhang, Konggang Qu, Guodong Shen, Huiyan Ma, Yuchao Li, et al. Layered and pb-free organic–inorganic perovskite materials for ultraviolet photoresponse:(010)-oriented (ch3nh3) 2mncl4 thin film. *ACS applied materials & interfaces*, 8(41):28187–28193, 2016.

[63] Daniele Cortecchia, Herlina Arianita Dewi, Jun Yin, Annalisa Bruno, Shi Chen, Tom Baikie, Pablo P Boix, Michael GraÌ́tzel, Subodh Mhaisalkar, Cesare Soci, et al. Lead-free $MA_2CuCl_xBr_{4-x}$ hybrid perovskites. *Inorganic chemistry*, 55(3):1044–1052, 2016.

[64] Aslihan Babayigit, Anitha Ethirajan, Marc Muller, and Bert Conings. Toxicity of organometal halide perovskite solar cells. *Nature materials*, 15(3):247, 2016.

[65] Lorna Fewtrell, Rachel Kaufmann, and Annette Prüss-Üstün. Assessing the environmental burden of disease at national and local levels. *Environmental burden of disease series*, (2), 2003.

[66] Peter Babington. *Code of Federal Regulations*, volume 29. Office of the Federal Register National Archives and Records Administrattion, 2005.

[67] Aslihan Babayigit, Dinh Duy Thanh, Anitha Ethirajan, Jean Manca, Marc Muller, Hans-Gerd Boyen, and Bert Conings. Assessing the toxicity of Pb-and Sn-based perovskite solar cells in model organism danio rerio. *Scientific reports*, 6:18721, 2016.

[68] Werner Kern et al. Handbook of semiconductor wafer cleaning technology. *New Jersey: Noyes Publication*, pages 111–196, 1993.

[69] John C de Mello, H Felix Wittmann, and Richard H Friend. An improved experimental determination of external photoluminescence quantum efficiency. *Advanced materials*, 9(3):230–232, 1997.

[70] Jan Ilavsky. Nika: software for two-dimensional data reduction. *Journal of Applied Crystallography*, 45(2):324–328, 2012.

[71] Ingo Breßler, Joachim Kohlbrecher, and Andreas F Thünemann. Sasfit: a tool for small-angle scattering data analysis using a library of analytical expressions. *Journal of applied crystallography*, 48(5):1587–1598, 2015.

[72] Ou Chen, Jing Zhao, Vikash P Chauhan, Jian Cui, Cliff Wong, Daniel K Harris, He Wei, Hee-Sun Han, Dai Fukumura, Rakesh K Jain, et al. Compact high-quality cdse–cds

core–shell nanocrystals with narrow emission linewidths and suppressed blinking. *Nature materials*, 12(5):445, 2013.

[73] Victor Malgras, Satoshi Tominaka, James W Ryan, Joel Henzie, Toshiaki Takei, Koji Ohara, and Yusuke Yamauchi. Observation of quantum confinement in monodisperse methylammonium lead halide perovskite nanocrystals embedded in mesoporous silica. *Journal of the American Chemical Society*, 138(42):13874–13881, 2016.

[74] Christian Wehrenfennig, Mingzhen Liu, Henry J Snaith, Michael B Johnston, and Laura M Herz. Homogeneous emission line broadening in the organo lead halide perovskite ch3nh3pbi3–x cl x. *The journal of physical chemistry letters*, 5(8):1300–1306, 2014.

[75] Aparna Shinde, Richa Gahlaut, and Shailaja Mahamuni. Low-temperature photoluminescence studies of cspbbr3 quantum dots. *The Journal of Physical Chemistry C*, 121(27):14872–14878, 2017.

[76] Vikash Kumar Ravi, Abhishek Swarnkar, Rayan Chakraborty, and Angshuman Nag. Excellent green but less impressive blue luminescence from cspbbr3 perovskite nanocubes and nanoplatelets. *Nanotechnology*, 27(32):325708, 2016.

[77] Stefano Sanguinetti, Mario Guzzi, and Massimo Gurioli. Accessing structural and electronic properties of semiconductor nanostructures via photoluminescence. In *Characterization of Semiconductor Heterostructures and Nanostructures*, pages 175–208. Elsevier, 2008.

[78] Jan Tauc. Optical properties and electronic structure of amorphous ge and si. *Materials Research Bulletin*, 3(1):37–46, 1968.

[79] Kai-Hung Wang, Liang-Chen Li, Muthaiah Shellaiah, and Kien Wen Sun. Structural and photophysical properties of methylammonium lead tribromide (mapbbr 3) single crystals. *Scientific reports*, 7(1):13643, 2017.

[80] Hong-Hua Fang, Sampson Adjokatse, Haotong Wei, Jie Yang, Graeme R Blake, Jinsong Huang, Jacky Even, and Maria Antonietta Loi. Ultrahigh sensitivity of methylammonium lead tribromide perovskite single crystals to environmental gases. *Science Advances*, 2(7):e1600534, 2016.

[81] Yuxi Tian, Maximilian Peter, Eva Unger, Mohamed Abdellah, Kaibo Zheng, Tõnu Puller-its, Arkady Yartsev, Villy Sundström, and Ivan G Scheblykin. Mechanistic insights into perovskite photoluminescence enhancement: light curing with oxygen can boost yield thousandfold. *Physical Chemistry Chemical Physics*, 17(38):24978–24987, 2015.

[82] Wei Zhang, Victor M Burlakov, Daniel J Graham, Tomas Leijtens, Anna Osherov, Vladimir Bulović, Henry J Snaith, David S Ginger, Samuel D Stranks, et al. Photo-induced halide redistribution in organic–inorganic perovskite films. *Nature communications*, 7:11683, 2016.

[83] Ruidong Zhu, Zhenyue Luo, Haiwei Chen, Yajie Dong, and Shin-Tson Wu. Realizing rec. 2020 color gamut with quantum dot displays. *Optics express*, 23(18):23680–23693, 2015.

[84] Johannes Schindelin, Ignacio Arganda-Carreras, Erwin Frise, Verena Kaynig, Mark Longair, Tobias Pietzsch, Stephan Preibisch, Curtis Rueden, Stephan Saalfeld, Benjamin Schmid, et al. Fiji: an open-source platform for biological-image analysis. *Nature methods*, 9(7):676, 2012.

[85] Tao Li, Andrew J Senesi, and Byeongdu Lee. Small angle x-ray scattering for nanoparticle research. *Chemical reviews*, 116(18):11128–11180, 2016.

[86] Jens Als-Nielsen and Des McMorrow. *Elements of modern X-ray physics*. John Wiley & Sons, 2011.

[87] Constantinos C Stoumpos, Christos D Malliakas, and Mercouri G Kanatzidis. Semiconducting tin and lead iodide perovskites with organic cations: phase transitions, high mobilities, and near-infrared photoluminescent properties. *Inorganic chemistry*, 52(15):9019–9038, 2013.

[88] Kenichiro Tanaka, Takayuki Takahashi, Takuma Ban, Takashi Kondo, Kazuhito Uchida, and Noboru Miura. Comparative study on the excitons in lead-halide-based perovskite-type crystals ch3nh3pbbr3 ch3nh3pbi3. *Solid state communications*, 127(9-10):619–623, 2003.

[89] G Porod. General theory. In *Small angle X-ray scattering*. 1982.

[90] Peter LAGGNER, Marlene STROBL, Philipp JOCHAM, Peter M ABUJA, and Manfred KRIECHBAUM. In-situ saxs on transformations of mesoporous and nanostructured solids. *Studies in surface science and catalysis*, pages 661–665, 2007.

[91] Owen D Miller, Eli Yablonovitch, and Sarah R Kurtz. Strong internal and external luminescence as solar cells approach the shockley–queisser limit. *IEEE Journal of Photovoltaics*, 2(3):303–311, 2012.

[92] Sjoerd A Veldhuis, Pablo P Boix, Natalia Yantara, Mingjie Li, Tze Chien Sum, Nripan Mathews, and Subodh G Mhaisalkar. Perovskite materials for light-emitting diodes and lasers. *Advanced Materials*, 28(32):6804–6834, 2016.

[93] L Turyanska, A Patane, M Henini, B Hennequin, and NR Thomas. Temperature dependence of the photoluminescence emission from thiol-capped pbs quantum dots. *Applied Physics Letters*, 90(10):101913, 2007.

[94] Kewei Wu, Ashok Bera, Chun Ma, Yuanmin Du, Yang Yang, Liang Li, and Tom Wu. Temperature-dependent excitonic photoluminescence of hybrid organometal halide perovskite films. *Physical Chemistry Chemical Physics*, 16(41):22476–22481, 2014.

[95] Zhuo Chen, Chonglong Yu, Kai Shum, Jian J Wang, William Pfenninger, Nemanja Vockic, John Midgley, and John T Kenney. Photoluminescence study of polycrystalline cssni3 thin films: Determination of exciton binding energy. *Journal of Luminescence*, 132(2):345–349, 2012.

[96] E Cohen, RA Street, and A Muranevich. Bound excitons and resonant raman scattering in cd x zn 1- x te (0.9âĽď xâĽď 1). *Physical Review B*, 28(12):7115, 1983.

[97] CJ Youn, TS Jeong, MS Han, and JH Kim. Optical properties of zn-terminated zno bulk. *Journal of Crystal Growth*, 261(4):526–532, 2004.

[98] P Lautenschlager, PB Allen, and M Cardona. Temperature dependence of band gaps in si and ge. *Physical Review B*, 31(4):2163, 1985.

[99] M Sebastian, JA Peters, CC Stoumpos, J Im, SS Kostina, Z Liu, MG Kanatzidis, AJ Freeman, and BW Wessels. Excitonic emissions and above-band-gap luminescence in the single-crystal perovskite semiconductors cspbb r 3 and cspbc l 3. *Physical Review B*, 92(23):235210, 2015.

[100] IP Pashuk, NS Pidzyrajlo, and MG Matsko. Exciton absorption, luminescence and resonance raman scattering in cspbcl 3 and cspbbr 3 crystals at low temperatures. *Fizika Tverdogo Tela*, 23(7):2162–2165, 1981.

[101] Shintaro Nomura and Takayoshi Kobayashi. Exciton–lo-phonon couplings in spherical semiconductor microcrystallites. *Physical Review B*, 45(3):1305, 1992.

[102] Constantinos C Stoumpos, Christos D Malliakas, John A Peters, Zhifu Liu, Maria Sebastian, Jino Im, Thomas C Chasapis, Arief C Wibowo, Duck Young Chung, Arthur J Freeman, et al. Crystal growth of the perovskite semiconductor cspbbr3: a new material for high-energy radiation detection. *Crystal Growth & Design*, 13(7):2722–2727, 2013.

[103] Weiguang Kong, Zhenyu Ye, Zhen Qi, Bingpo Zhang, Miao Wang, Arash Rahimi-Iman, and Huizhen Wu. Characterization of an abnormal photoluminescence behavior upon crystal-phase transition of perovskite ch 3 nh 3 pbi 3. *Physical Chemistry Chemical Physics*, 17(25):16405–16411, 2015.

[104] Lin Ma, Feng Hao, Constantinos C Stoumpos, Brian T Phelan, Michael R Wasielewski, and Mercouri G Kanatzidis. Carrier diffusion lengths of over 500 nm in lead-free perovskite ch3nh3sni3 films. *Journal of the American Chemical Society*, 138(44):14750–14755, 2016.

[105] Thirumal Krishnamoorthy, Hong Ding, Chen Yan, Wei Lin Leong, Tom Baikie, Ziyi Zhang, Matthew Sherburne, Shuzhou Li, Mark Asta, Nripan Mathews, et al. Lead-free germanium iodide perovskite materials for photovoltaic applications. *Journal of Materials Chemistry A*, 3(47):23829–23832, 2015.

[106] Xianxi Zhang, Jie Yin, Zhonghao Nie, Qian Zhang, Ning Sui, Baoli Chen, Yingtian Zhang, Konggang Qu, Jinsheng Zhao, and Huawei Zhou. Lead-free and amorphous organic–inorganic hybrid materials for photovoltaic applications: mesoscopic ch 3 nh 3 mni 3/tio 2 heterojunction. *RSC Advances*, 7(59):37419–37425, 2017.

[107] H Arend, W Huber, FH Mischgofsky, and GK Richter-Van Leeuwen. Layer perovskites of the (cnh2n+ 1nh3) 2mx4 and nh3 (ch2) mnh3mx4 families with m= cd, cu, fe, mn or pd and x= cl or br: Importance, solubilities and simple growth techniques. *Journal of Crystal Growth*, 43(2):213–223, 1978.

Stepan Demchyshyn

stepan.demchyshyn@jku.com • +43 677 619 66697

Education

Master Degree Program in Technical Chemistry   2016 – present
Johannes Kepler University Linz (JKU)   Linz, Austria

Bsc in Biological Chemistry   2012 – 2016
University of South Bohemia (USB)   Ceske Budejovice, Czech Republic

Joined degree between Johannes Keler University (JKU), Linz, Austria and University of South Bohemia (USB), Budweis, Czech Republic

Publications

S. Demchyshyn, J. Roemer, H. Groiß, H. Heilbrunner, C. Ulbricht, D. Apaydin, A. Böhm, U. Rütt, F. Bertram, G. Hesser, M. Scharber, N. S. Sariciftci, B. Nickel, S. Bauer, E. D. Glowacki, M. Kaltenbrunner, *Confining metal-halide perovskites in nanoporous thin films*. Science Advances, (2017).

V. Derek, E. D. Glowacki, M. Bednorz, S. Demchyshyn, N.S. Sariciftci, M. Ivanda, *Nano-and micro-structured silicon/organic hybrid near-infrared photodetectors*. SPIE Photonics Europe (2016)

Theses

Bachelor thesis   Microwave-assisted Kjeldahl determination of total nitrogen in food and other samples

Bachelor thesis   Further Delineation of *Borrelia burgdorferi* Restriction-Modification system and understanding antibiotic resistance in *Borrelia afzelii*

Experience

Student Assistant   March 2017 – current
Departement of Soft Matter Physics in Experimental Physics Institute (SoMaP), JKU   Linz, Austria
Investigating various solid state matrices for quantum confinement of organolead hybrid perovskites and their application in light emitting diodes.

Intern   Jun 2016 – May 2017
Research and Development, Surface Department, voestalpine Steel Division   Linz, Austria
Developing tests and methods for investigation of surface properties for high strength steel for energy and construction industry.

Student Assistant   Nov 2015 – Aug 2016
Phyiscal Chemistry Institute/Linz Institute of Organic Solar Cells (LIOS), JKU   Linz, Austria
Nanostructuring of aluminum and silicon oxide for device fabrication.

Teaching Assistant   Mar 2015 – Jun 2015
Institute of Analytical Chemistry, JKU   Linz, Austria
Assisted first year students in their introductory Analytical Chemistry Laboratory Course

Conferences

Floating gate field-effect sensors employing porous aluminum oxide poster at BioEl2016 International Winterschool on Bioelectronics, Kirchberg in Tirol, Austria, 2016

Scholarships

Cultural exchange Received a scholarship by U.S. Department of State to participate in Future Leader Exchange Program in Fairfax, VA, USA in 2010/2011, where acquired crucial intercultural, communication, and volunteering skills.